Geomechanics for Energy and the Environment 29 (2022) 100272

Contents lists available at ScienceDirect

Geomechanics for Energy and the Environment

journal homepage: www.elsevier.com/locate/gete

Effect of pore fluid chemistry on uniaxial compaction creep of Bentheim sandstone and implications for reservoir injection operations

M.T.W. Schimmel[1], S.J.T. Hangx*, C.J. Spiers

High Pressure and Temperature Laboratory, Department of Earth Sciences, Faculty of Geosciences, Utrecht University, Utrecht, The Netherlands

ARTICLE INFO

Article history:
Received 14 January 2021
Received in revised form 3 August 2021
Accepted 3 September 2021
Available online 16 September 2021

Editors-in-Chief:
Professor Lyesse Laloui and Professor Tomasz Hueckel

Keywords:
Fluid–rock interaction
Geological storage
Fluid injection
Stress corrosion cracking
Time-dependent deformation

ABSTRACT

In the transition to a sustainable energy system, natural gas may be an interim source for relatively low-carbon energy production. However, hydrocarbon production worldwide is leading to reservoir compaction and, consequently, surface subsidence and induced seismicity, hampering the potential of natural gas. Reservoir compaction may potentially be mitigated by fluid injection. Fluid injection into porous subsurface reservoirs is also required in other technologies envisioned in a sustainable energy system, such as geothermal energy production and temporary storage of renewable energy. However, fluid injection into porous reservoirs may create a chemical disequilibrium between the pore fluid and host rock, potentially activating fluid–rock interactions that can cause compaction of the reservoir. These chemically activated fluid–rock interactions are not well-understood, and, therefore, we performed uniaxial compaction experiments at 35, 75 and 100 MPa effective stress, employing samples of Bentheim sandstone saturated with supercritical phases (i.e. N_2, CO_2, wet-N_2 and wet-CO_2), distilled water and aqueous solutions (i.e. 3.7 pH HCl solution, AMP solution and $AlCl_3$ solution), as well as low-vacuum (dry) conditions. Creep strain and acoustic emissions (AEs) accumulated with increasing stress and sample porosity. While saturation with supercritical fluids produced slightly less creep strain than dry conditions, flooding with distilled water doubled the creep strain. The acidic solutions inhibited compaction creep compared to distilled water saturation. AE activity and microstructural analysis revealed that microcracking controlled deformation, presumably via stress corrosion cracking. While the supercritical fluids may have dried crack tips, distilled water likely reduced the stress required for Si-O bond breakage. The acidic solutions inhibited microcracking through, presumably, a change in surface energy. Our results suggest that fluids devoid of water, with low water content or acidic in nature can be injected into quartz-rich porous reservoirs without increasing reservoir compaction rates.

1. Introduction

Natural gas is expected to play an important interim role during the transition from fossil fuels to sustainable energy as a lower carbon alternative to coal and oil.[1] However, prolonged production of hydrocarbons can lead to unwanted phenomena such as surface subsidence and induced seismicity.[2–6] The occurrence of such phenomena in gas fields or in depleted reservoirs used to store natural gas could reduce the potential for natural gas to contribute to the energy transition. To limit the impact of natural gas production, particularly from smaller fields, a variety of concepts have been proposed for injecting fluids into the reservoir to mitigate reservoir compaction, either through pressure restoration[3,7] or chemical manipulation.[8] Any of such actions clearly requires a firm understanding of the mechanical response of the reservoir rock.

Subsurface fluid injection into aquifers and depleted hydrocarbon reservoirs also plays an important role in other strategies to reduce carbon emissions, notably in the context of geothermal electricity generation and geothermal heating of homes and building infrastructure.[1,9] In addition, depleted hydrocarbon reservoirs are targeted for permanent disposal of wastewater[10] and CO_2, and for temporary storage of renewable energy[11] in the form of synthetic fuels,[12] compressed air,[13] or hydrogen.[14] In principle, all of these activities can potentially induce environmental and/or geological risks.[15,16] Induced seismicity is frequently observed in areas of active wastewater injection[17,18] and in the vicinity of geothermal projects.[19,20] Furthermore, injected fluids have the potential to leak, leading to economic loss[21]

* Corresponding author.
E-mail address: s.j.t.hangx@uu.nl (S.J.T. Hangx).
[1] Now at: Ministry of Economic Affairs and Climate, The Hague, The Netherlands.

https://doi.org/10.1016/j.gete.2021.100272

and/or environmental impact.[22–24] To avoid these unwanted effects it is once again important to understand the response of the reservoir rock to the mechanical and chemical changes caused by fluid injection.

Fluid production or injection affects the pore pressure (P_p) in the reservoir rock relative to the constant overburden stress (σ_v), changing the effective stress acting on the reservoir rock, according to Terzaghi's effective stress principle $\sigma_{v,eff} = \sigma_v - P_p$. Consequently, the reservoir rock may respond poro-elastically,[25,26] thus affecting the state of stress in and around the reservoir. However, other effects, which are less well-understood, include permanent (inelastic) deformation of the reservoir, in response to increased contact stresses during fluid extraction,[27–30] or to changes in the chemical environment during fluid injection and resulting fluid–rock interactions.[8] These changes may activate processes leading to time-independent or even time-dependent permanent deformation of the reservoir rock, such as intergranular sliding, grain rotation and rearrangement,[31–34] brittle failure of grains and grain contacts,[28,35–37] intergranular clay film deformation,[27,38] stress-driven solution transfer[39–42] and mineral dissolution/reaction due to fluid disequilibrium.[43,44]

Much work has been done on the deformation behaviour of reservoir rocks in response to applied stress, temperature and chemical environment. Experiments have been performed on loose sands[8,33,36,37,45–48] and sandstones.[28,29,35,49–61] However, most studies to date have employed either air dry samples[8,33,36,37,45,48] or samples with water as pore fluid,[8,28,29,35–37,45–61] leaving the effects of other chemically active fluid compositions, particularly on sandstone deformation behaviour, poorly explored.[8,37,45,48] Moreover, creep experiments on sandstones under varying chemical conditions are few and rarely conducted under zero lateral strain conditions expected in situ.[62]

To contribute to this latter knowledge gap, we conducted compaction creep experiments on clean, quartz-rich, Bentheim sandstone in a uniaxial compaction vessel (oedometer), imposing zero lateral strain conditions, using tightly fitting samples jacketed in a thin polymer sleeve. A range of pore fluids, including dry and wet supercritical N_2 and CO_2, and aqueous solutions, were employed to investigate the effect of chemical environment on compaction creep under drained conditions. The chemical environments were selected based on a previous study investigating the impact of fluids on compaction of loose quartz sand.[8] The experiments were performed at a typical reservoir temperature of 80 °C (i.e. 2–4 km depth, assuming a geothermal gradient of 20–40 °C/km), and at constant axial effective stresses of 35, 75 and 100 MPa. The experiments showed that 1-D compaction creep is strongly influenced by pore fluid chemistry, increasing with the activity of water and/or the pH of the fluid moving from dry and wet supercritical fluids to low-vacuum (dry) conditions to acidic aqueous solutions to distilled water. Acoustic emission data and microstructural analysis revealed that microcracking was the dominant deformation mechanism. The results imply that injection into quartz-rich reservoirs of fluids devoid of water or characterised by low water content, and acidic fluids would decrease reservoir compaction rates.

2. Experimental method

2.1. Sample and pore fluid preparation

Cylindrical samples were cored from outcrop blocks of Bentheim sandstone, retrieved from the Gildenhausen quarry near the village of Bentheim, Germany. This sandstone was selected as it has been extensively studied and is well-known for its relatively homogeneous composition, consisting mainly of quartz grains and quartz cement.[55,63–77] No bedding was apparent in either the starting blocks or the cored samples. The cores were 19.6 mm in diameter and approximately 50 mm in length. The porosity of all cores was determined using gravimetric methods, by weighing the samples dry and saturated with water. Together with the core dimensions, this yielded porosities of 21.8–23.3% (Table 1). After porosity determination, the cores were cut into shorter cylindrical plugs of approximately 10 mm length. The ends of each plug were ground flat and perpendicular to the sample axis.

In total, 14 uniaxial creep experiments were performed on such plugs, whereby three control experiments were done under low-vacuum (dry) conditions. In addition, eight different chemical environments were employed to investigate the effect of chemical environment on compaction creep (Table 1). Four supercritical phases were employed at a fluid pressure (P_p) of 10 MPa, including N_2 (purity $\geq$ 99.999 vol %), CO_2 (purity $\geq$ 99.7 vol %), water-saturated-N_2 (wet-N_2), and water-saturated-CO_2 (wet-CO_2). In addition, two 'simple' aqueous solutions (HCl solution of pH 3.7 and distilled water) and two 'complex' solutions were used, at atmospheric pressure. The complex solutions consisted of a widely used scaling inhibitor solution containing 0.004 M AMP (amino trimethylene phosphonic acid; pH 2.5) and a 0.01 M $AlCl_3$ solution (pH 2.8).

Low-vacuum (dry) conditions were obtained by evacuating the sample within the oedometer compaction vessel before and during mechanical testing, using a single-stage rotary vacuum pump (Fig. 1a). Dry supercritical fluids were prepared by filling an ISCO pump (total volume 68 mL) with pure N_2 or CO_2. These were then pre-pressurised to 9 MPa using a diaphragm pump (Fig. 1a). The externally heated ISCO pump was then used to achieve further pressurisation to 10 MPa at 60 °C, resulting in supercritical conditions.[78] Wet-N_2 or wet-CO_2 phases were prepared by filling the ISCO pump with a small volume of water (10 mL) and filling the remaining volume with pure N_2 or CO_2, respectively. The mixture was then pre-pressurised to 9 MPa using the diaphragm pump and further pressurisation to 10 MPa was achieved using the ISCO pump, while heating to 60 °C. This procedure yielded a maximum water concentration at 60 °C of 9.1 mol of water/m^3 for the wet-N_2 and 33.8 mol/m^3 for the wet-CO_2 (see Refs. 8, 78–80). All supercritical fluids were prepared at 60 °C as opposed to the experimental conditions of 80 °C to protect the seals of the ISCO pump and prevent condensation of water in the wet phases upon injection into the sample. Prior to injection into the sample, the fluids were left to equilibrate overnight.

The HCl solution of pH 3.7 was prepared by diluting a fixed quantity of hydrochloric acid (HCl) in distilled water. The 0.004 M AMP solution was prepared by diluting 1 ‰ AMP solution with 1 L of distilled water and for the 0.01 M $AlCl_3$ solution, 2.4143 g of aluminium chloride salt was dissolved in 1 L of distilled water. All of these acidic aqueous solutions were stirred for approximately 5 mins and left to equilibrate for at least 5 days prior to use. After equilibration, each solution was heated to 80 °C before measuring solution pH using a portable pH meter (Oakton Instruments) that accounts for the temperature-dependence of pH.

2.2. Experimental set-up and acoustic monitoring system

The sandstone compaction experiments were performed in a uniaxial (1-D) compaction vessel (oedometer), secured in an Instron 8862 servo-controlled loading frame (Fig. 1b and c). The compaction vessel is modified from the vessel originally described by Ref. 39. This vessel was previously used for compaction experiments on loose granular material.[8,36,37,45,48] In the present study, the vessel was employed for uniaxial compaction testing of tight-fitting sandstone plugs (prepared as described above) jacketed in a thin polymer sleeve, under zero radial strain boundary

Table 1
Overview of uniaxial compaction experiments on Bentheim sandstone in this study, all at 80 °C.

Experiment	ϕ_i [%]	Chemical environment	Fluid pH	σ_{eff} [MPa]	Characteristic stiffness [GPa]	Duration creep phase [h]	ε_c [%]
Control experiments							
unconstrained	22.3	low-vacuum (dry)	–	62[a]	7.0 ± 0.0	–	–
loadunload	22.3	low-vacuum (dry)		100	10.1 ± 0.0	–	–
dry01	22.2	low-vacuum (dry)	–	35	–	43	0.05
dry02	22.3	low-vacuum (dry)	–	75	7.9 ± 0.1	94	0.10
dry03	22.2	low-vacuum (dry)	–	100	7.8 ± 0.1	43	0.21
Supercritical fluids (P_p = 10 MPa)							
N202	21.8	N_2	–	100	8.5 ± 0.1	41	0.15
wN201[b]	22.3	wet-N_2	–	100	9.3 ± 0.1	68	0.31
CO202	22.5	CO_2	–	100	8.3 ± 0.7	43	0.17
CO203	21.8	CO_2	–	100	10.3 ± 0.1	42	0.09
wCO201	22.3	wet-CO_2	–	100	9.6 ± 0.1	44	0.15
Aqueous solutions (atmospheric pore pressure)							
DI01	22.3	distilled water	5.9	75	7.5 ± 0.8	64	0.23
DI02	22.2	distilled water	5.9	100	9.6 ± 0.1	87	0.48
3HCl01	21.8	HCl solution	3.7	100	10.6 ± 0.1	41	0.18
AMP01	23.3	AMP solution	2.5	100	6.0 ± 0.0	43	0.51
AMP02	22.4	AMP solution	2.5	100	8.9 ± 0.1	44	0.29
AlCl301	22.4	$AlCl_3$ solution	2.8	100	8.1 ± 0.1	67	0.25

Note. φ_i denotes initial sample porosity as determined prior to testing through gravimetric methods, σ_{eff} applied effective stress, ε_c is the strain accumulated during creep.
[a]Effective stress at failure.
[b]Ingress of distilled water after approximately 25 h of creep.

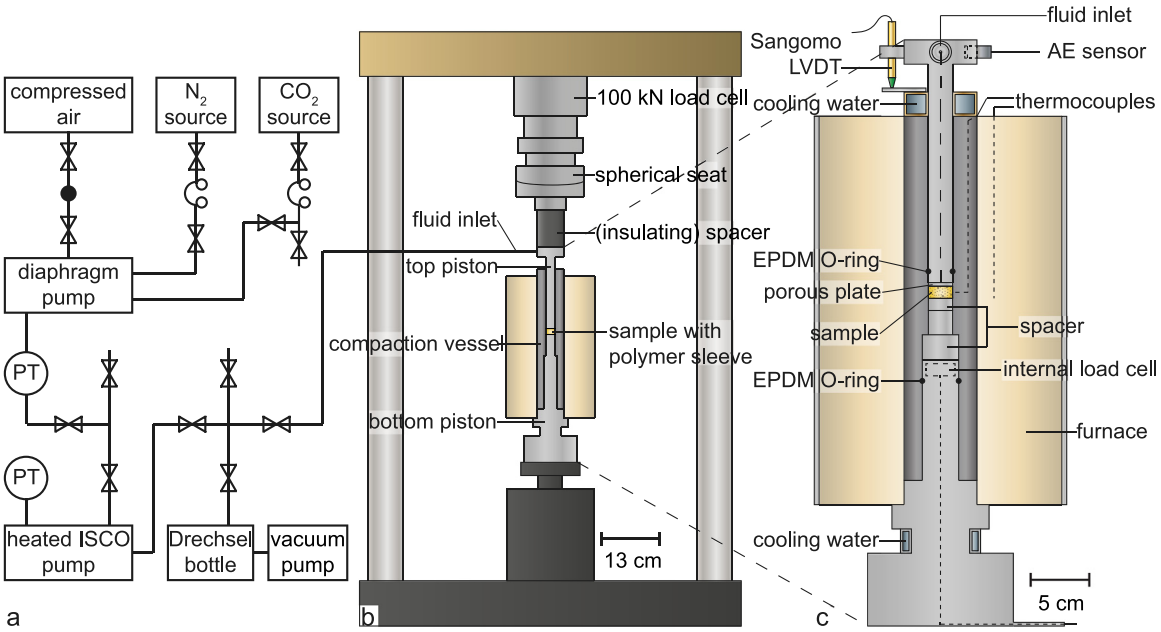

Fig. 1. Overview of the experimental set-up used in this study (from Schimmel, Hangx, et al.[8]). (a) Pore fluid system including a diaphragm pump, servo-controlled ISCO pump, Drechsel bottle and vacuum pump. Fluid pressure was measured using pressure transducers denoted PT. (b) Instron servo-controlled loading frame employed with a 100 kN load cell and (c) compaction vessel.

conditions. The radial (effective) stress was accordingly (near) zero at zero axial load, increasing with loading but unmeasured.

The vessel and loading pistons are constructed from corrosion resistant Monel K-500, a copper–nickel–molybdenum alloy. The top piston contains a pore fluid bore, allowing both evacuation of the sample and injection of a pore fluid. A 1 mm thick, porous, stainless steel plate between the top piston and sample ensures even distribution of fluid over the sample cross-sectional area upon fluid injection. In addition, it prevents loose sandstone grains from entering and clogging the pore fluid bore. Both the top and bottom piston are sealed against the vessel wall using EPDM O-rings.

Axial force, displacement and temperature are controlled and measured throughout the experiment. Force is applied by advancing the Instron loading ram. It is measured externally using the Instron load cell (0–100 kN range, resolution ± 0.05 kN). In addition, force is measured with an internal load cell (0–100 kN range, resolution ± 0.05 kN) located in the top part of the bottom piston. Piston position and displacement are measured using a linear variable differential transformer (LVDT) located in the Instron drive unit (± 50 mm range, resolution ± 0.25 μm) and a Sangamo LVDT (± 1 mm range, resolution ± 0.1 μm) located between the upper piston and the vessel (Fig. 1c). A furnace allows controlled heating of the sample with ± 0.5 °C accuracy using a K-type chromel-alumel control thermocouple. This thermocouple is positioned within the furnace windings and connected to

a proportional–integral–derivative (PID) controller. A second K-type thermocouple, embedded in the vessel wall adjacent to the sample, independently measures sample temperature.

In addition, the experimental set-up is equipped with an acoustic emission (AE) monitoring system that detects and counts AEs produced by the compacting sample.[8] The AE events are detected using a ceramic piezoelectric resonator, mounted externally on the top piston (Fig. 1c). The resulting signal passes through a precision preamplifier (36 dB gain) and a multistage signal conditioning system (24 dB gain). A 100 kHz to 1 MHz band-pass filter is applied to eliminate low frequency interference and sensor resonance effects. Lastly, a two-counter channel with a constant trigger-threshold of 200 mV, which is just above the noise level, discriminates and counts the incoming AE events. Pulse stretching times (PST) of 1000 μs and 500 μs are set for each counter, to check for wave pocket arrival-bouncing effects and counter saturation. In case of discrete events, the count rates from the two channels should be identical.

Sample evacuation and fluid introduction are achieved via the pore fluid system (Fig. 1a). This consists of a vacuum pump, Drechsel bottle, ISCO pump, diaphragm pump, and sources of compressed air (0.8 MPa), N_2 and CO_2 (bottle pressures of 20 and 5.7 MPa, respectively). The vacuum pump is connected to the sample via the Drechsel bottle for evacuation of the sample. The diaphragm pump is used for pre-pressurising the fluids in the ISCO pump at 9 MPa. The ISCO pump is used to achieve further pressurisation to 10 MPa, while heating to 60 °C. Via the combination of valves shown in Fig. 1, the sample can be directly connected to the ISCO pump to inject fluids prepared in the ISCO pump. Alternatively, the sample can be connected to the Drechsel bottle for vacuum-flooding with aqueous solutions. Pore fluid pressure is controlled at 10 ± 0.14 MPa using the ISCO pump.

2.3. Experimental procedure

2.3.1. Control experiments

Prior to the sandstone experiments with different chemical environments, a series of experiments was conducted to test whether the tight-fitting samples would be effectively constrained to (near) zero radial strain. In these control experiments, we deformed two aluminium samples with known elastic properties, as well as two Bentheim sandstone samples, under radially unconstrained (no jacket) and radially constrained (with tight-fitting jacket) conditions, at 80 °C. The aim was to compare the constrained and unconstrained elastic stiffness parameters for aluminium and Bentheim sandstone to measured values. Theoretically, the axial stiffness of an unconstrained sample is represented by the Young's modulus (E). By contrast, for a fully constrained sample, the stiffness is represented by the constrained modulus (M), which can be calculated using the Young's modulus and Poisson's ratio (ν) using the relation

$$M = \frac{E\,(1-\nu)}{(1+\nu)\,(1-2\nu)} \quad (1)$$

For aluminium, the Young's modulus ranges from 68 to 70 GPa and the Poisson's ratio from 0.33 to 0.346,[81–83] yielding an M value in the range 101 to 110 GPa. For Bentheim sandstone, the Young's modulus lies in the range 8.9 to 14.7 GPa, while the Poisson's ratio is reported to be 0.13–0.36,[65,67,75] which would give M = 9.3 to 17.6 GPa.

For the unconstrained test on Bentheim sandstone, the sample was used as prepared, i.e. we used an unjacketed plug, 10 mm in length and 19.6 mm in diameter, which is slightly smaller than the 20 mm diameter vessel chamber. The aluminium sample used in the unconstrained test on this material was unjacketed and 19.5 mm in diameter and also 10 mm in length. This sample was slightly smaller in diameter to compensate for the larger coefficient of thermal expansion of aluminium ($\alpha_{aluminium}$ = 23 · 10^{-6} °C^{-1}; Ref. 81) compared to sandstone ($\alpha_{Bentheim}$ = 10.9 · 10^{-6} °C^{-1}; Ref. 66), ensuring the sample remained unconstrained during heating to 80 °C. For the constrained tests, a 19.6 × 10mm Bentheim plug was used as prepared, along with an aluminium sample of the same dimension. Both samples were jacketed with a fluorinated ethylene propylene (FEP), heat shrink sleeve of 200 μm thickness to make the sample fit exactly in the vessel. The FEP-sleeve, with a coefficient of thermal expansion (α_{FEP}) of 135 · 10^{-6} °C^{-1}, compensated for the differential thermal expansion between the aluminium dummy sample or Bentheim sandstone sample and the compaction vessel (α_{Monel} = 13.7 · 10^{-6} °C^{-1}) during heating to 80 °C, ensuring continued tightfitting of the sample in the vessel. Before testing, the jackets were sprayed with Molykote D-312R, to reduce friction between the sample and the vessel wall, and the spray was allowed to dry for at least one hour.

Prior to inserting the sample into the compaction vessel, the vessel was mounted on its lower piston. A 10 mm high stainless steel spacer was emplaced in the vessel to position the sample in the centre of the vessel, and the (un)jacketed sample and porous steel plate inserted. The furnace and top piston were subsequently added and the entire assembly located in the Instron loading frame.

2.3.2. Experiments on constrained sandstone samples using different chemical environments

In preparation for each experiment, the sample was jacketed in a FEP sleeve and located into the 1-D compaction vessel and Instron loading frame as described above. The compaction vessel was then heated to the target temperature of 80 °C in approximately 2 h, while simultaneously evacuating the sample assembly. After reaching the target temperature, a small stress of 0.3 MPa (equivalent to a load of 0.1 kN) was applied to the sample. In the case of the low-vacuum (dry) experiments, a loading ramp was applied with a constant stress rate of 5 MPa/min, corresponding to loading strain rates in the range 1.5 · 10^{-5} to 2.0 · 10^{-5} s^{-1}, to attain a constant applied stress of 35, 75 or 100 MPa (Table 1).

A slightly different approach was used for the experiments employing a high-pressure pore fluid. After insertion of the sample and installation of the apparatus in the Instron frame, a 3 mm gap was created between the upper piston spacing block and the Instron load cell (see Fig. 1). Then, the pressurised fluid (P_p = 10 MPa) was introduced. After pore pressure stabilisation (1–2 mins), the top piston was slowly advanced (1 mm/min) to apply a small load to the sample (touch position). During slow piston advancement to this position, dynamic seal friction was determined in the presence of the high-pressure fluid, being 0.4–0.8 MPa. Subsequently, a loading ramp of 5 MPa/min was initiated to increase the applied stress to 110.4–110.8 MPa, such that the effective stress on the sample was 100 MPa.

Samples tested with aqueous pore fluids at atmospheric conditions were first vacuum-flooded with the pore fluid, at a small applied stress of 0.3 MPa. The pore fluid pressure was maintained at atmospheric pressure by drainage to air. After flooding, the applied stress was increased to 75 or 100 MPa (Table 1) at 5 MPa/min. In all experiments, the creep phase was taken to commence at the moment the final constant stress was reached on the sample.

The creep phase lasted up to 94 h, after which each test was terminated (see Table 1). Experiments performed at low-vacuum (dry) conditions were completely unloaded at 5 MPa/min, followed by removal of the vacuum. Samples saturated with pressurised fluids were first unloaded (5 MPa/min) to their original

touch position, and after removing the pore pressure, the samples were fully unloaded. Vacuum-saturated samples were fully unloaded at a rate of 5 MPa/min, maintaining drainage to atmospheric pressure. After unloading, the furnace was switched off and the samples were left to cool to room temperature. Finally, the assembly was removed from the Instron loading frame and the samples were carefully extracted. Wet samples were placed in an oven at 50 °C to dry for a minimum of five days prior to preparation for microstructural analysis.

2.4. Data acquisition and processing

Throughout each experiment, external Instron load, internal load, Instron LVDT position, Sangamo LVDT position, sample temperature and cumulative acoustic emission count were logged at an interval of one second. Applied axial stress and effective axial stress were calculated from the external Instron load and internal load data, using pore fluid pressure data where relevant. Friction between the top piston seal and vessel wall was considered negligible for all experiments (< 0.8 MPa – see above). However, comparison of external and internal load cell data indicated measurable sample-vessel wall friction. The difference between the external and internal stress was smallest in the experiments conducted with pressurised pore fluids, e.g. at 100 MPa effective stress, the stress measured by the internal load cell varying between 99.4 and 102.4 MPa. For experiments conducted at low-vacuum (dry) conditions or with aqueous solutions at atmospheric pressures, the internal axial stress measured between 94.5 and 98.4 MPa at 100 MPa applied stress. Taking the sample stress as the average of the internally and externally measured stress yields an average (effective) sample stress of 101.0 ± 0.9 MPa for samples employing pressurised pore fluids, and 98.4 ± 1.0 MPa for dry and vacuum-saturated samples. On this basis, sample-vessel wall friction is assumed to be < 2.6% of the applied effective stress in all cases.

Sample length was measured prior to testing using a calliper, as well as by comparing the Instron LVDT position to an empty vessel reference point. Though both approaches yielded similar results, the latter was preferred as this allowed calculation of the instantaneous sample length. Both the Instron LVDT position and the Sangamo LVDT displacement data were corrected for elastic machine distortion using a predefined, eighth-order polynomial function determined from machine calibrations on the experimental set-up without a sample. In addition, the time and Sangamo LVDT displacement data was time-averaged over a window of 60 s to reduce noise in the data. From the corrected and averaged displacement data, instantaneous volumetric strain, defined as $e_v \approx -\Delta L/L_0$, was calculated, where L_0 is the length of the sample at the start of the loading or creep phase and ΔL is the change in sample length at any subsequent instant. The corrected and averaged time and displacement data measured during the creep phase were used to calculate instantaneous strain rates defined as $\dot{\varepsilon} = -(1/L)(dL/dt)$. The strain rates were calculated by performing a least-squares inversion over a variable time window centred around each individual displacement data point. The window size was based on a set displacement tolerance of 4 μm. Though this method allowed for accurate determination of both high and low strain rates, large errors were found towards the end of several experiments when the displacement resolution (±0.1 μm) of the Sangamo LVDT was reached. Therefore, strain rates with an error of more than 1.5% and/or rates below $10^{-8.0}$ s^{-1} were excluded from further analysis. Similarly, instantaneous AE rates were calculated from the cumulative AE count data, with the tolerance for the AE window size set to 200 AE events.

In addition, the axial sample stiffness during loading was evaluated for each sample. The characteristic sample stiffness is defined as the slope of the linear part of the stress–strain curve during loading, determined via linear least-squares regression. In the current experiments, the stress–strain curve was nonlinear at stresses below 30 MPa, and hence the characteristic sample stiffness was determined for higher stresses (see Fig. 2a and c).

2.5. Analytical and microstructural methods

After drying, all samples, except dry01, CO202 and AMP01, were impregnated with a low-viscosity, blue-dyed (Oil Blue organic dye, DuPont), epoxy resin (Araldite 2020) for microstructural analysis. Thin sections (∼30 μm thick) were cut parallel to the loading axis and analysed using transmitted light microscopy. The blue-dyed resin resulted in a clear distinction between pores and grains. Micrograph mosaics (50 × magnification; 9 by 18 mm) covering the entire thin section were obtained to qualitatively investigate the grain-scale mechanisms controlling deformation.

3. Results

3.1. Control experiments on unconstrained vs. constrained samples

The results of our control experiments performed on aluminium and sandstone samples to investigate if the FEP-sleeve approach would effectively constrain tight-fitting samples to (near) zero radial strain are shown in Fig. 2. In both the constrained and unconstrained experiments using aluminium dummies, the samples were loaded and unloaded in six cycles up to a maximum applied axial stress of 55 MPa under lab dry conditions at 80 °C. Both samples showed a highly compliant, non-linear stress–strain response (Fig. 2a) up to ∼10 MPa, followed by rapid stiffening in the range 10–20 MPa. This likely reflects stiffening of the machine related to increased alignment at higher stresses. Above 30 MPa (dashed horizontal line in Fig. 2a), the stress–strain response approached linear behaviour, which enabled us to determine the characteristic stiffness of the dummy samples for each stress-cycle in the range 30–55 MPa. This varied over the six stress-cycles applied (Fig. 2b), with the unconstrained and constrained aluminium sample showing a stiffness of approximately 70 GPa and 144 GPa, respectively.

The results obtained in the unconstrained and constrained control tests performed using Bentheim sandstone at low-vacuum (dry) conditions and 80 °C are shown in Fig. 2c and d. Only one loading cycle was applied in these runs. For reference, the loading data of experiment dry02 is added to these figures, because it had the same starting porosity and was conducted under the same conditions. Overall, the stress–strain behaviour of the sandstone samples showed similar characteristics to the aluminium dummy at axial stresses up to ∼60 MPa, with the exception that the stiffness was much lower. Between 30 and 60 MPa (dashed horizontal lines in Fig. 2c), the stress–strain response of the unconstrained and constrained samples approached linear behaviour, such that the characteristic stiffness of the sandstone samples could be determined in the range 30–60 MPa. The characteristic stiffness of the unconstrained sandstone samples was 7.0 ± 0.0 GPa, while the constrained samples had higher stiffness values of 10.1 ± 0.0 GPa (loadunload) and 7.9 ± 0.1 GPa (dry02, see Table 1). As can be seen, the unconstrained sample (grey line in Fig. 2c) failed at approximately 62 MPa applied stress, indicated by the rapid increase in strain and deviation from linearity of the stress–strain curve. This was accompanied by a surge in AE activity (Fig. 2d). The FEP-constrained sandstone sample did not show this type of behaviour, as evidenced by the much lower AE count (16,000 AE counts versus 65,000 AE counts when unconstrained).

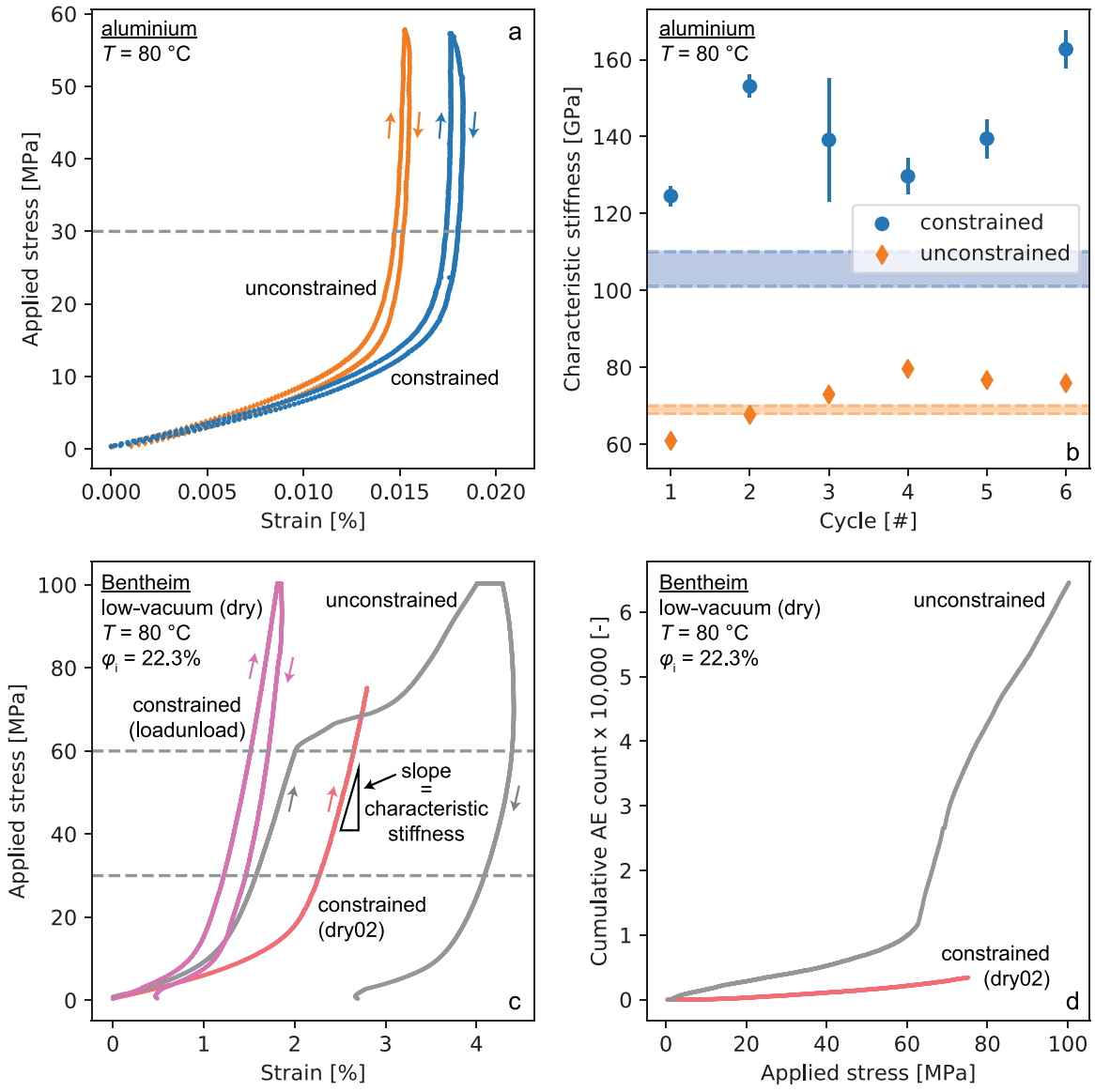

Fig. 2. Loading and unloading data of FEP-constrained and unconstrained aluminium and Bentheim sandstone samples at 80 °C. (a) Stress–strain curves reflecting the first stress-cycle of the aluminium samples. Note the non-linearity up to 30 MPa (vertical dashed line). (b) Characteristic stiffness of the aluminium samples, determined at applied stresses above 30 MPa for each cycle. Error bars indicate the 95% confidence interval, which is in some cases smaller than the symbol size. The orange and blue zones indicate the range of literature values for the unconstrained (Young's modulus, E = 68–70 GPa) and constrained modulus (M = 101–110 GPa) for aluminium, respectively. (c) Stress–strain curves and (d) cumulative AE count during loading for the unconstrained and constrained (loadunload and dry02) sandstone samples under low-vacuum (dry) conditions. Note AEs were not recorded in the loadunload test. T denotes temperature, φ_i initial sample porosity and AE acoustic emission.

3.2. Deformation of constrained sandstone samples during loading

For the active loading phase of the experiments, the strain versus applied axial stress behaviour observed for the constrained samples exposed to different chemical environments is similar to that observed in the control experiments (Fig. 3a and b; cf. Section 3.1). Most experiments fall in the strain range of 1.8–2.4% at the end of the loading stage, with the exception of experiments dry01, dry02, DI01, CO203 and AMP01, which all showed strains approximately 0.5% higher. The experiments employing super-critical fluids generally showed a more rapid increase in strain for the first few MPa of stress applied to the sample. There does not appear to be a systematic effect of fluid on the strain achieved during loading though it is noteworthy that, in the low-vacuum (dry) experiments, the onset of audible AEs is evident at much lower applied stresses than in the fluid-saturated experiments (see Fig. 3c and d).

The characteristic stiffness of each sample was determined from a linear fit to the stress–strain data in the applied effective stress range 30 to 60 MPa and yielded values between 6.0 and 10.6 GPa. Note that experiment dry01 was excluded from this analysis, because it was only loaded to 35 MPa. The stiffness appeared to be independent of water concentration (Fig. 3e) and fluid pH (Fig. 3f). By contrast, sample porosity, despite falling in a narrow range of 21.8–23.3%, appeared to impact the amount of total strain obtained during loading, with the higher porosity samples CO202 (φ_i = 22.5%) and AMP01 (φ_i = 23.3%) being more compliant, with characteristic stiffness of 8.3 ± 0.7 and 6.0 ± 0.0 GPa, than their lower porosity counterparts CO203 (φ_i = 21.8%) and AMP02 (φ_i = 22.4%) with stiffness values of 10.3 ± 0.1 and 8.9 ± 0.1 GPa, respectively (see Fig. 3e and f).

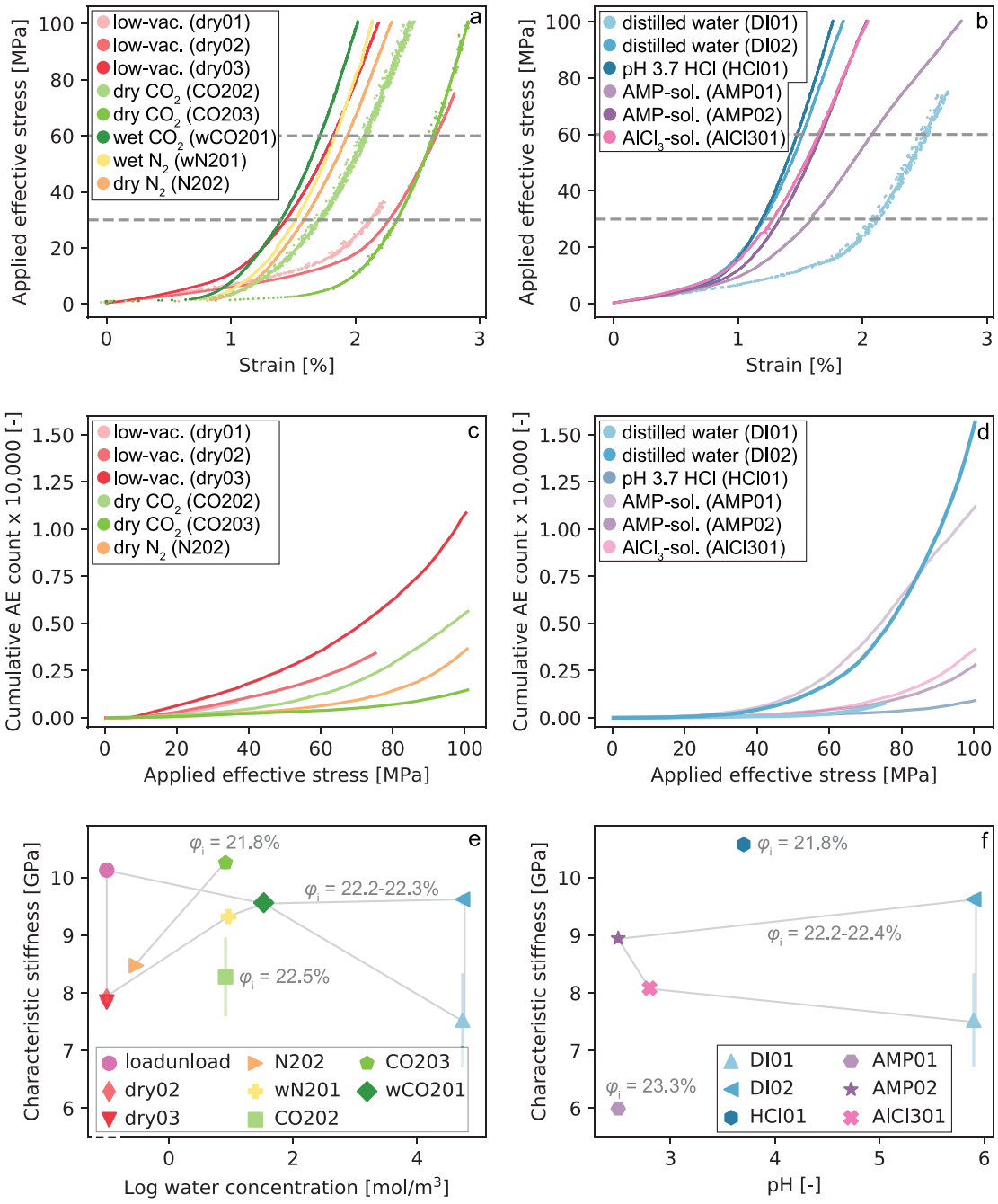

Fig. 3. Mechanical and acoustic data for the FEP-jacketed (laterally constrained) Bentheim sandstone samples during active loading under low-vacuum (dry) conditions and saturated with supercritical fluids or aqueous solutions. All experiments were loaded with an axial loading rate of 5 MPa/min, corresponding to loading strain rates in the range $1.5 \cdot 10^{-5}$ to $2.0 \cdot 10^{-5}$ s^{-1}. (a and b) Stress–strain curves. (c and d) Cumulative AE count during loading. (e) Characteristic stiffness determined using a linear fit to the data shown in a and b between 30 and 60 MPa effective stress as a function of (e) water concentration and (f) as a function of solution pH. Error bars indicate the 95% confidence interval, which is in some cases smaller than the symbol size. Porosity is indicated and tie lines are added between samples with similar porosity. Samples and corresponding pore fluid conditions are identified in Table 1. AE data was most likely improperly recorded during the HCl, AMP and $AlCl_3$ solution experiments, hence the lighter shaded curves and labels.

3.3. Compaction creep at different applied stresses and low-vacuum (dry) vs. wet conditions

The compaction creep data obtained for the sandstone samples after loading to a constant applied (effective) stress of 35, 75 and 100 MPa at low-vacuum (dry) conditions, and 75 and 100 MPa applied stress at fluid-saturated (distilled water) conditions are presented in Fig. 4. All experiments showed rapid accumulation of strain in the first few minutes after attaining the creep testing stress, followed by ongoing deformation at decreasing strain rates (Fig. 4a and c). The AE data showed a similar response versus time and strain (c.f. Fig. 4a and b, and Fig. 4c and d). Note that for an applied stress of 35 MPa under dry conditions, almost no strain and no AE counts were accumulated during the creep phase, excluding reliable calculation of strain rate and AE rate.

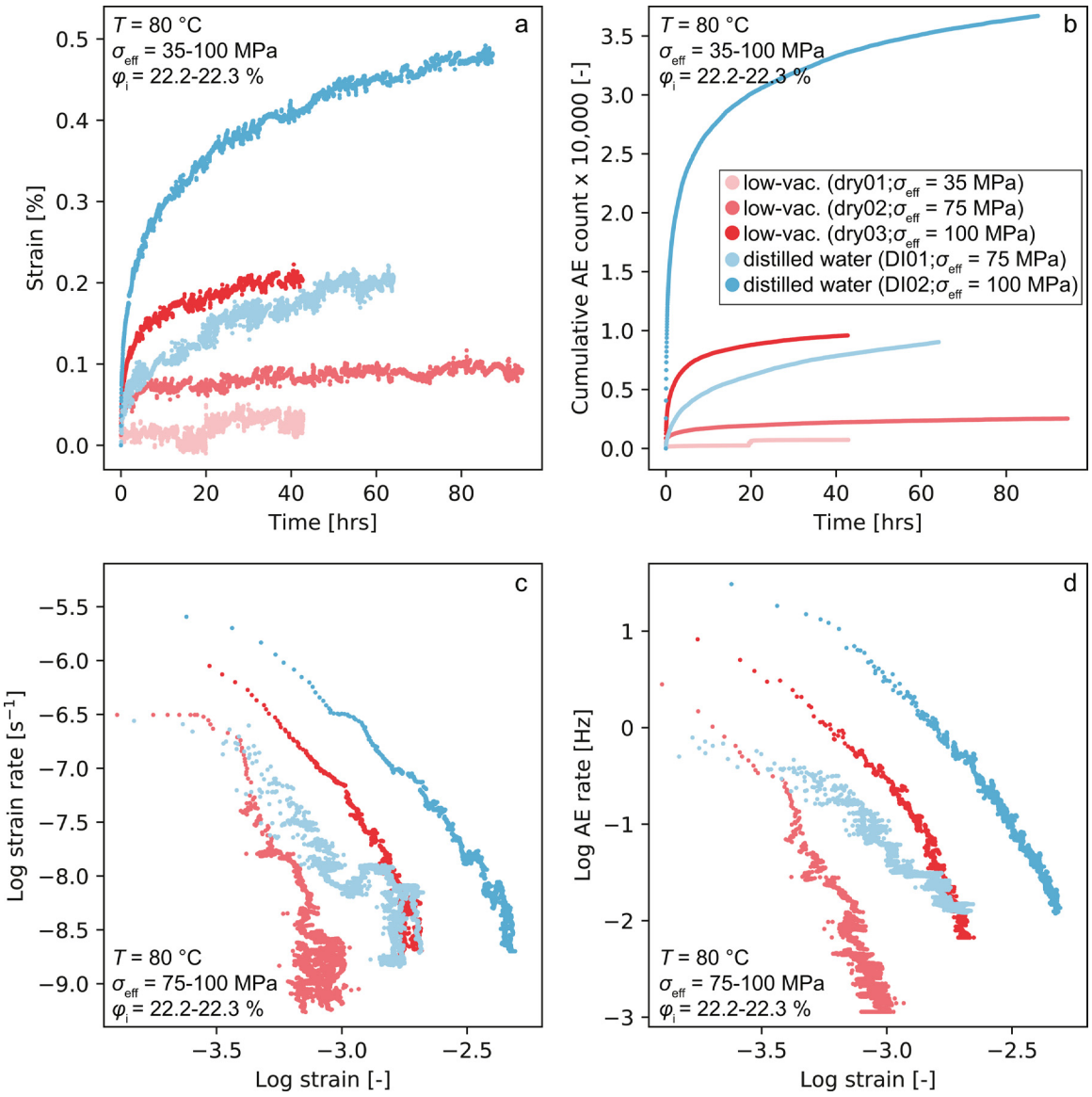

Fig. 4. The effect of applied stress and low-vacuum (dry) versus fluid-saturated (distilled water) on compaction creep in Bentheim sandstone. (a) Strain and (b) cumulative AE count versus time. (c) Log strain rate and (d) log AE hit rate as a function of log strain. Note that the creep and AE rates could not be calculated for the dry experiment conducted at 35 MPa, due to insufficient compaction over time. T denotes temperature, σ_{eff} effective stress and φ_i initial sample porosity. The applied stress is indicated in brackets for each experiment. The zero reference is the start of the creep phase, i.e. the moment a constant stress is applied to the sample.

As expected, creep strains and cumulative AE count increased with increasing applied stress (Fig. 4a and b). After 40 h of compaction at low-vacuum (dry) conditions, the total creep strain amounted to 0.02, 0.09 and 0.2% at 35, 75 and 100 MPa applied stress, respectively (Fig. 4a). A similar trend was observed in the AE counts, with almost no AEs counted at 35 MPa applied stress, and approximately 2,200 and 9,500 AEs counted at 75 and 100 MPa applied stress, respectively (Fig. 4b).

Furthermore, at given applied stress, more creep strain and AEs were measured in samples saturated with distilled water compared to dry conditions (Fig. 4a and b). After 40 h under distilled water conditions, creep strain was roughly double the strain measured under dry conditions, amounting to 0.17 and 0.41% at 75 and 100 MPa applied stress, respectively (Fig. 4a). This increase in strain was also reflected in the cumulative AE data, with 3.5 times more AEs counted during wet creep, i.e. approximately 7,800 and 33,300 counts at 75 and 100 MPa applied stress, respectively (Fig. 4b).

Similarly, strain rates increased with applied stress and saturation of the sample with distilled water, and, for all samples, creep strain rates decreased with accumulating strain (Fig. 4c). At 75 MPa applied stress, initial strain rates were roughly similar ($10^{-6.6}$-$10^{-6.5}$ s^{-1}) for the dry and wet sample, but as compaction increased, creep under dry conditions slowed down more rapidly with strain, compared to fluid-saturated conditions. By contrast, at 100 MPa applied stress, initial strain rates were higher under fluid-saturated conditions compared to the dry environment, measuring $10^{-6.0}$ and $10^{-5.6}$ s^{-1} for the dry and distilled water sample, respectively. This behaviour was also reflected in the AE rate data (Fig. 4d), with higher AE count rates being measured at larger applied stress and under distilled water-saturated conditions (Fig. 4d). Initially, i.e. up to 0.03% strain ($10^{-3.55}$), the 75 MPa distilled water experiment showed a slightly lower AE count rate ($10^{0.4}$ s^{-1}) and strain rate than the 75 MPa dry experiment. At 100 MPa applied stress, AE rates of $10^{1.4}$ and $10^{1.8}$ s^{-1} were measured in the dry and wet sample, respectively, in line with

the higher strain rates obtained for the distilled water-saturated samples (cf. Fig. 4c). Interestingly, the decrease in strain rate and AE rate with strain seen in the dry experiments appeared to be more rapid than for the fluid-saturated experiments.

The close correlation between strain and AE count is explicitly shown in Fig. 5, where cumulative AE count and AE rate are plotted as a function of strain and strain rate, respectively. A linear relation between AE count and strain was observed for all applied stresses in both the low-vacuum (dry) and distilled water-saturated conditions (Fig. 5a). In addition, AE rate showed a linear dependency on strain rate, which can be approximated by a slope of 1 for all dry and distilled water-saturated samples (Fig. 5b).

In short, our experiments indicated that creep strain, AE count, creep rates and AE rates strongly increased with increasing applied stress, and with the addition of distilled water. Creep and AE rates were approximately one order of magnitude faster at 100 MPa applied stress than at 75 MPa (Fig. 4c and d).

3.4. Compaction creep in different chemical environments

3.4.1. Compaction creep in supercritical fluids

Bentheim sandstone samples saturated with supercritical fluids at 10 MPa pore pressure (N_2, wet-N_2, CO_2 and wet-CO_2) showed compaction creep behaviour similar to that observed for dry and water-saturated samples, with an initial rapid increase in strain, followed by a slowing down of the creep rate (Fig. 6). Note that the sudden increase in strain and strain rate around 25 h in the wet-N_2 experiment was caused by ingress of distilled water due to a leaking pore fluid system. AE data was not recorded in the wet-N_2 and wet-CO_2 experiment due to technical issues.

It can be noted that samples saturated with supercritical fluids displayed less creep strain and fewer AEs than samples loaded under dry conditions. In addition, a small effect of sample porosity was observed, with creep strain and AEs increasing with porosity (cf. CO202 and CO203). Focusing on the samples with a porosity of 22.2–22.5%, after 20 h of creep, the samples saturated with wet-N_2, CO_2 and wet-CO_2 displayed similar amounts of creep strain, ranging from 0.11 to 0.13% (Fig. 6a), which was less than the amount of strain measured for the dry sample (0.18%). Note that for similar sample porosities there is no significant difference in the strain accumulated in the presence of wet-CO_2 compared to wet-N_2. For samples with a slightly lower porosity (φ_i = 21.8%), saturation with CO_2 produced less creep strain (CO203; 0.08%) than saturation with N_2 (0.12% strain). The observed strain-time behaviour in response to different chemical environments was also reflected in the cumulative AE data (Fig. 6b). While almost 9,000 AE counts were registered in the dry sample at 20 h, 3,000 AEs were measured in the higher porosity CO_2 experiment (CO202), and 3,500 and a little over 1,000 AEs in the lower porosity N_2 and CO_2-saturated samples (CO203).

Strain rates and AE rates in samples saturated with supercritical fluids were lower overall than the rates measured for a dry environment (Fig. 6c and d). Initial strain rates ranged from $10^{-6.8}$ to $10^{-6.0}$ s^{-1} and decreased as creep strain accumulated. For the slightly lower porosity samples (φ_i = 21.8%), the reduction in strain rate with strain appeared to be more rapid than for the more porous samples (φ_i = 22.2–22.5%), i.e. a strain exponent of −4.2 to −5.6 s^{-1} compared to −2.6 to −3.4 s^{-1}. AE rates in all experiments decreased from initial values of approximately 10^1 s^{-1} to final values at test termination of 10^{-2} s^{-1} (Fig. 6d). Though overall AE rate was highest in the dry experiments, it displayed the most rapid reduction with increasing strain. The lowest reduction in AE rate with strain was observed for the high porosity CO_2-saturated sample (CO202). The low porosity N_2 and CO_2-saturated (CO203) samples displayed an intermediate reduction in AE rate with increasing strain.

Overall, the presence of supercritical fluids caused less compaction and slower creep rates than seen under dry conditions (Fig. 6). It should be noted, the compaction behaviour significantly changed in experiment wN201, where, after 25 h of creep, water leaked into the sample. This led to a marked increase in strain and strain rate (Fig. 6a and c). After the initial surge in strain rate upon water ingress, the strain rate decayed to rates similar to before after approximately 0.2% of strain. This behaviour is in accordance with that observed when comparing individual dry and water-saturated experiments (cf. Section 3.3).

3.4.2. Compaction creep in acidic aqueous solutions

Samples flooded with acidic aqueous solutions (pH 3.7 HCl solution, pH 2.5 AMP solution, pH 2.8 $AlCl_3$ solution) displayed typical compaction creep behaviour similar to that exhibited by the dry, distilled water-saturated and supercritical fluid-saturated samples (Fig. 7). In the porosity range 22.2–22.4%, samples saturated with acidic solutions showed less creep strain and fewer accumulated AEs, and lower creep strain rates and AE rates than the sample tested with distilled water at 100 MPa stress (Fig. 7). However, the introduction of acidic fluid still led to more deformation compared to the vacuum-dry environment.

After 40 h of compaction and focusing on the experiments in the porosity range 22.2–22.4%, the lowest creep strain was measured in the $AlCl_3$ solution experiment (0.22%), while the AMP solution-saturated sample exhibited 0.28% strain. Overall, less creep strain was produced in the acidic environments compared to distilled water (0.41% strain). This influence of chemical environment was also reflected in the strain rate data. Initial creep strain rates were between $10^{-6.0}$ and $10^{-5.6}$ s^{-1}, and reduced with ongoing creep (Fig. 7c). The decrease in strain rate was faster in the acidic environments (strain exponent of −3.9 and −4.3 s^{-1} for AMP02 and AlCl301, respectively) than in the dry (strain exponent of −3.4 s^{-1}), and the water-saturated environments (strain exponent of −2.8 s^{-1}).

Besides the effect of chemical environment, porosity played a role in controlling the amount of strain and the strain rate. In accordance with previous observations (cf. N202 and CO203), this is illustrated by experiments 3HCl01 (φ_i = 21.8%) and AMP01 (φ_i = 23.3%), which employed samples with the lowest and highest porosity of the batch, respectively. The sample saturated with pH 3.7 HCl solution (3HCl01) produced the smallest amount of creep strain (Fig. 7a), while the strain measured for the more porous AMP01 sample was almost double (0.51%) compared to its 22.4% porosity equivalent (AMP02; Fig. 7a). The influence of porosity is also reflected in the strain rate data, as evidence by lower and higher strain rates for 3HCl01 and AMP01, respectively, compared to the samples in the porosity range 22.2–22.4% (Fig. 7c).

Unfortunately, a problem with the AE sensor was noted after the experiments with acidic aqueous solutions were conducted, suggesting that the AE counts may have been impeded due to insufficient contact of the piezoelectric resonator with the vessel. This may explain why the cumulative AE counts recorded in the experiments conducted with acidic aqueous solutions were lower than expected based on the creep strain data and compared with the number of AEs recorded in the dry and wet reference experiments (Fig. 7b – note that for these experiments the curves are lighter shaded). However, the AE data qualitatively matched the trends observed in the strain data, i.e. the highest number of AEs were seen in the higher porosity AMP solution-flooded sample, intermediate values were obtained for the lower porosity AMP solution experiment and $AlCl_3$-saturated sample, and the lowest number of AE's was obtained in the pH 3.7 HCl solution experiment. In summary, the mechanical and AE data show the same trends, in that flooding of the Bentheim sandstone with acidic aqueous solution (HCl, AMP, $AlCl_3$ solution) inhibited compaction creep and creep strain rates (Fig. 7), compared to distilled water.

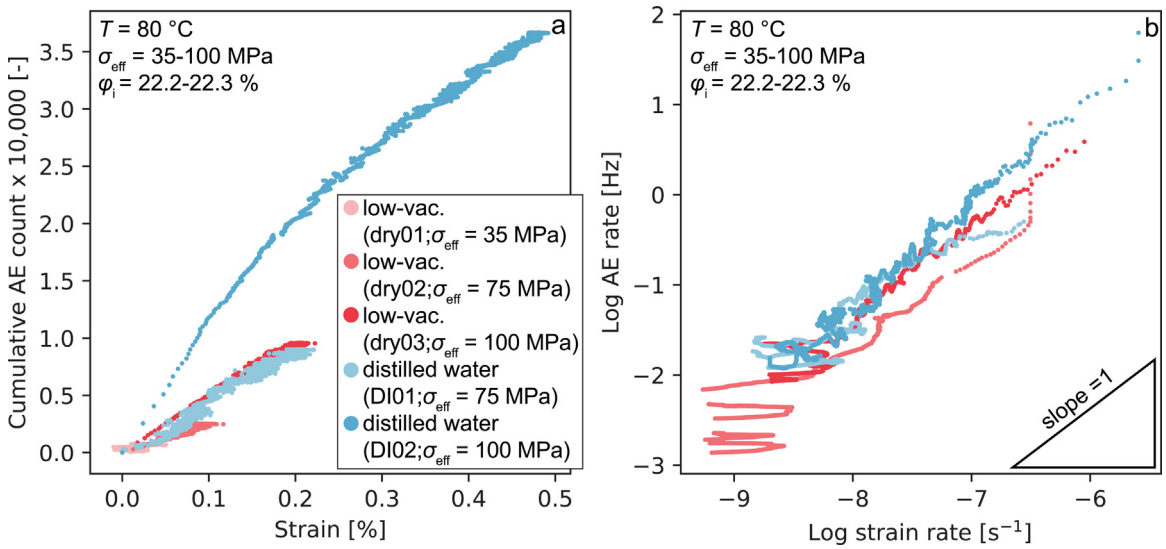

Fig. 5. Cumulative AE count and strain data collected during compaction creep of low-vacuum (dry) and distilled water-saturated Bentheim sandstone samples at applied stresses of 35, 75 and 100 MPa. (a) Cumulative AE counts versus strain. (b) Log AE rate versus log strain rate. Note that the creep and AE rates could not be calculated for the dry experiment conducted at 35 MPa, due to insufficient compaction over time. The zero reference is the start of the creep phase, i.e. the moment a constant stress is applied to the sample.

3.5. Microstructural data

A single undeformed Bentheim sandstone sample was analysed using optical microscopy. Manual counting of the grains confirmed that 95% of the grains consisted of quartz. The remaining grains consisted of corroded feldspar (~4%), partly altered to clay minerals. Primary clay minerals were also present and lined the pores in some areas (< 1%). The quartz grains were rounded to subrounded and ranged from 70 to 450 μm in diameter, with a mean grain size of 180–250 μm. Grain contacts generally appeared be (near-)point contacts (e.g. seen on right off centre in Fig. 8a), though to sutured, flattened contacts were also present (e.g. top left in Fig. 8a). Furthermore, the quartz grains contained fluid inclusions and occasionally pre-existing cracks, presumably resulting from its burial and diagenetic history (Fig. 8a). No bedding, laminations or grain sorting were visible.

One sample was loaded to 100 MPa and then directly unloaded (loadunload – see Table 1). Throughout this sample, more cracks were observed than in the undeformed sample (cf. Fig. 8a and b), however, cracks were not as abundant as seen in the samples that were also allowed to creep at constant stress (see Fig. 8c–g). Most cracks emanated from grain-to-grain contacts, both within grains (intergranular cracks, Fig. 8a–f), across grains (transgranular cracks, Fig. 8d–g), and along grain boundaries producing grain boundary breakage (Fig. 8c and f). Generally, cracks were oriented parallel or subparallel to the loading direction and not specifically related to the grain composition (quartz vs. feldspar). Though cracks were observed throughout the entire cross section of each sample, clusters of more severely damaged grains were also observed in samples AlCl301, AMP02, DI01, DI02 and wN201. These damage zones were a few grains wide and typically contained a large portion of crushed grains, in addition to cracked grains (Fig. 8e and f). These clusters of crushed grains formed circular patches and did not extend laterally to form bands.

4. Discussion

4.1. Deformation mechanisms responsible for compaction creep

We observed that creep was enhanced by increasing applied stress and by saturating the sample with distilled water or aqueous solutions. Together with (a) the AE activity observed during creep (Figs. 4, 6 and 7), (b) the linear relation observed between AE rate and strain rate, which was characterised by a slope of 1 (Fig. 5b), and (c) microstructural analysis, which showed an abundance of new cracks in the quartz grains post-creep deformation, it is inferred that compaction creep was accommodated by microcracking in quartz grains and breakage of cemented grain contacts with serial rearrangement of grains and grain fragments. Alternative deformation mechanisms include mass transfer processes such as dissolution of grains or of microscale asperities within grain contacts, or else pressure solution at grain contacts.[40,42,84] However, given the short duration of our experiments (less than 4 days), the relatively low temperature of the tests, the slow kinetics of these processes,[42] plus the lack of dissolution features in our deformed samples, we believe that any contribution of dissolution–precipitation mechanisms to deformation was likely negligible.

The cracks radiating from grain contacts in the quartz grains (Fig. 8) are typically referred to as Hertzian contact fractures.[37,85,86] These fracture develop at the edge of grain-to-grain contacts, where tensile stresses are largest (Hertzian contact theory[87]; see also Ref. 88). When a sample containing pre-existing flaws or cracks at grain surfaces is loaded, these cracks will propagate either in equilibrium Griffith mode or in a sub-critical time-dependent manner.[89,90] Equilibrium crack growth (Griffith criterion) occurs if the strain energy release rate G can provide the energy needed to form fracture surfaces, i.e. when $G = G_c = 2\gamma$, where γ is the (effective) surface energy per unit area [J m^{-2}] and G_c is the critical value of G, the fracture energy. Equivalently, the stress field around the crack tip can be described through the stress intensity factor K_I, while the material's resistance to crack propagation is given by the fracture toughness K_{IC},[91] so that crack growth occurs when $K_I = K_{IC}$. For a small, mode I (opening mode) crack, $K_I = Y\sigma_r (\pi c)^{1/2}$, where Y is a dimensionless factor equal to 1.12 for an edge crack, σ_r is the remotely applied stress [MPa] and c is the half-length of the flaw or crack [μm].[85,92,93] In line with the fact that K_{IC} is related to the energy release rate according to $G_c = K_{IC}^2 \left(1 - \upsilon^2\right)/E$,[93] equilibrium crack growth occurs $K_I = K_{IC} = (2E\gamma/\pi c)^{1/2}$.[94,95].

In a chemically active environment, cracks can grow subcritically (i.e. with $K_I < K_{IC}$ or $G < G_c$) via the process of stress corrosion.[96–99] The strained crack tips are more reactive

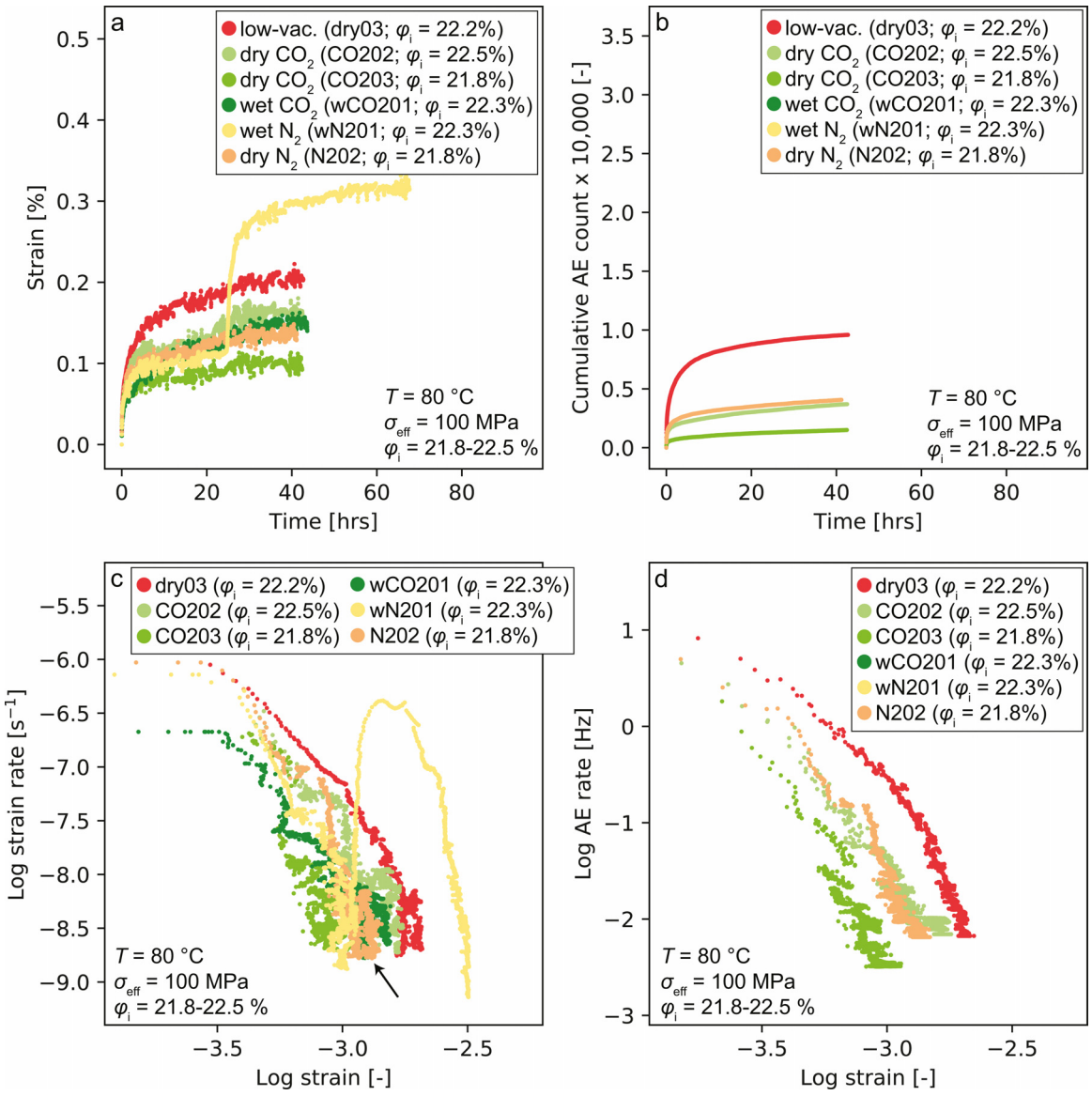

Fig. 6. Compaction creep in Bentheim sandstone saturated with N_2, wet-N_2, CO_2 or wet-CO_2. Sample compacted under low-vacuum (dry) conditions is added for reference. (a) Total strain and (b) cumulative AE count versus time. (c) Log strain rate and (d) log AE hit rate as a function of log strain. T denotes temperature and σ_{eff} effective stress. For each experiment, initial sample porosity φ_i is indicated, with all samples falling within the porosity range 21.8–22.5%. Note that AE data could not be collected during the wet-N_2 and wet-CO_2 experiments. The zero reference is the start of the creep phase, i.e. the moment a constant stress is applied to the sample.

due the large stress concentrations.[98,100–104] Corrosive species may, therefore, adsorb at the strained crack tip, reducing the energy required to create new fracture surface area.[92,105] In quartz, adsorption of or attack by corrosive species, such as water or hydroxyl groups, at the crack tip, cause the Si-O bond to be hydrolysed, creating silanol surface groups (SiOH). These reactions can be expressed as

$$> Si - O - Si < + H_2O = 2 > SiOH, \text{ for water adsorption} \quad (2)$$

and

$$> Si - O - Si < + OH^- = > SiOH + > SiO^-, \text{ for hydroxyl adsorption} \quad (3)$$

where < or > indicate surface-bound species.[106–109] The newly formed surface groups are weakly bonded by hydrogen bonds, which require less energy to break, facilitating crack propagation. At stress levels below those required for critical crack growth ($K_I < K_{IC}$ or $G < G_c$), the rate of crack growth depends on either the rate of transport of corrosive species to the crack tip or the kinetics of the bond hydrolysis reaction.[93]

Subcritical crack growth velocities in quartz and glass are known to be accelerated by increasing temperature,[93,110,111] humidity or water content[112–116] and solution pH.[99,106,117,118] Though it is challenging to measure crack growth velocities in sandstone samples,[93,119] similar effects of humidity and water have been observed,[120–122] Moreover, the influence of stress, temperature, water content and solution pH on compaction creep have been investigated for quartz sand aggregates[8,37,45,47] and to a limited extent sandstones,[55,58,123] and show that compaction creep rates increase when these variables increase. These trends are in line with our observations (Figs. 4 to 6), further supporting our inference that microcracking is the key mechanism controlling creep in our experiments.

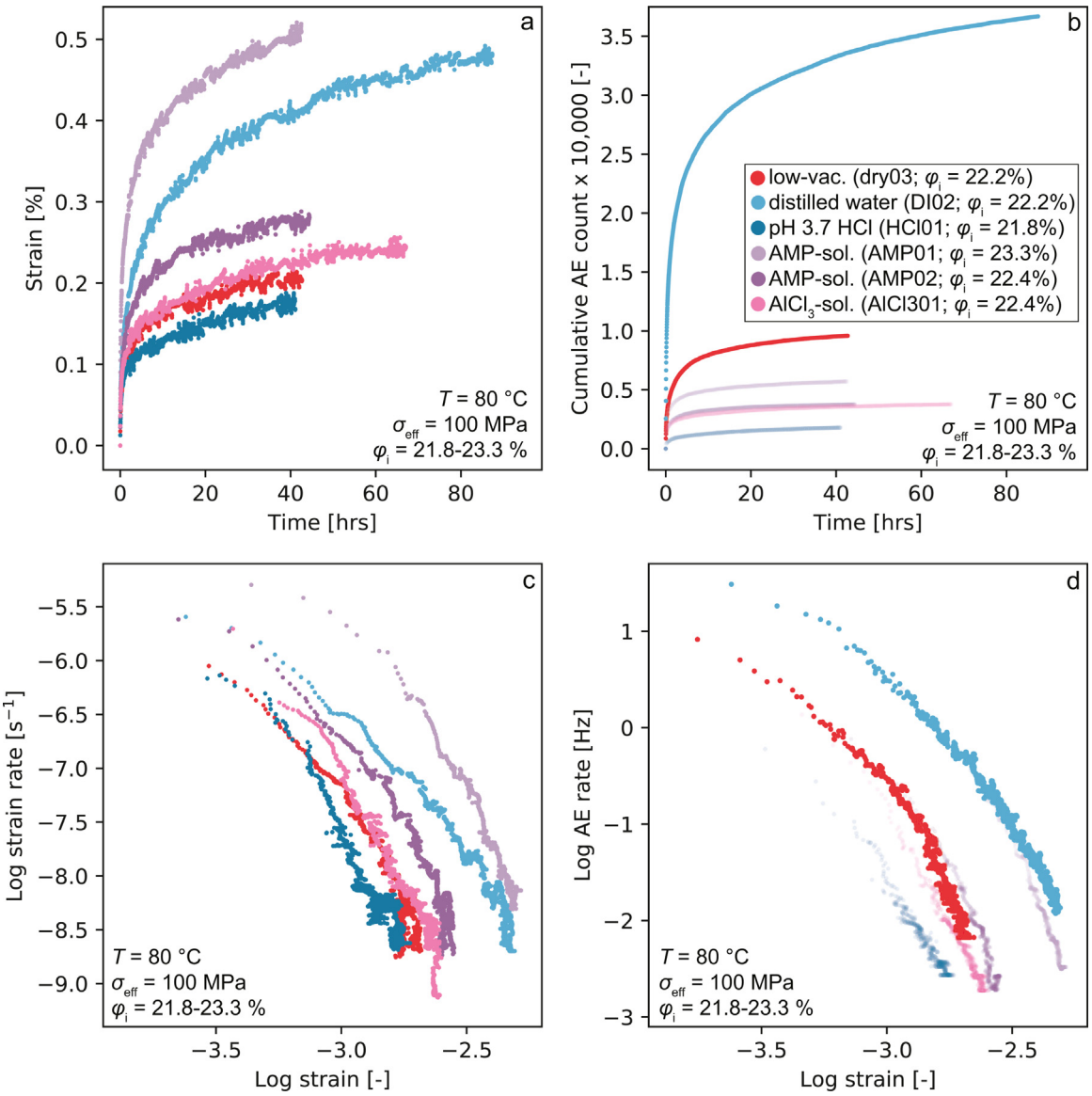

Fig. 7. Compaction creep in Bentheim sandstone saturated with pH 3.7 HCl solution, AMP solution (pH 2.5) or $AlCl_3$ solution (pH 2.8). Sample compacted under low-vacuum (dry) conditions and saturated with distilled water are added for reference. (a) Total strain and (b) cumulative AE count as a function of time. (c) Log strain rate and (d) log AE hit rate as a function of log strain. T denotes temperature and σ_{eff} effective stress. For each experiment, initial sample porosity φ_i is indicated, with all samples falling within the porosity range 21.8–23.3%. AE data was most likely improperly recorded during the HCl, AMP and $AlCl_3$ solution experiments, hence the lighter shaded curves and labels. The zero reference is the start of the creep phase, i.e. the moment a constant stress is applied to the sample.

4.1.1. The influence of applied stress and porosity on compaction creep

As shown in Fig. 4, creep strain, AE count, creep rates and AE rates strongly increase with increasing applied stress. At higher applied stresses, the stresses acting across grain-to-grain contacts are larger, in turn enhancing the stresses acting at crack tips, thereby promoting (subcritical) crack growth and compaction creep.

Our results also suggested that sample porosity exerted some influence on compaction creep behaviour. In samples saturated with dry supercritical CO_2, the sample with 0.7% higher porosity (21.8 vs. 22.5% porosity) showed creep strain rates and AE rates approximately half an order of magnitude faster than the lower porosity sample (Fig. 6c and d). Similarly, in samples with AMP solution as pore fluid, the sample with a higher porosity by 0.9% (22.4 vs. 23.3% porosity) creep strain rates were approximately one order of magnitude faster in the higher porosity sample (Fig. 7c). Most likely small differences in contact area or contact structure/cementation can explain the effect of porosity on creep rates, as these would lead to differences in stress intensity at crack tips, as well as the stress distribution around the crack tip, hence affecting crack propagation. However, we did not systematically investigate the effect of porosity on creep behaviour, so cannot infer more at present.

4.1.2. The influence of supercritical fluids on compaction creep

The influence of supercritical fluids on compaction creep at 100 MPa effective stress is explicitly shown in Fig. 9, where strain at fixed moments in time and strain rates at fixed strain are plotted as a function of water concentration. Fig. 9a and c show that even when the water concentration in the supercritical fluids increases, creep strain and strain rates do not, compared with low-vacuum (dry) conditions. By comparison, pore saturation with distilled water (DI) did lead to higher creep strains and higher strain rates. In the case of low-vacuum dry conditions, the sample, and therefore the crack tip, is not actively dried

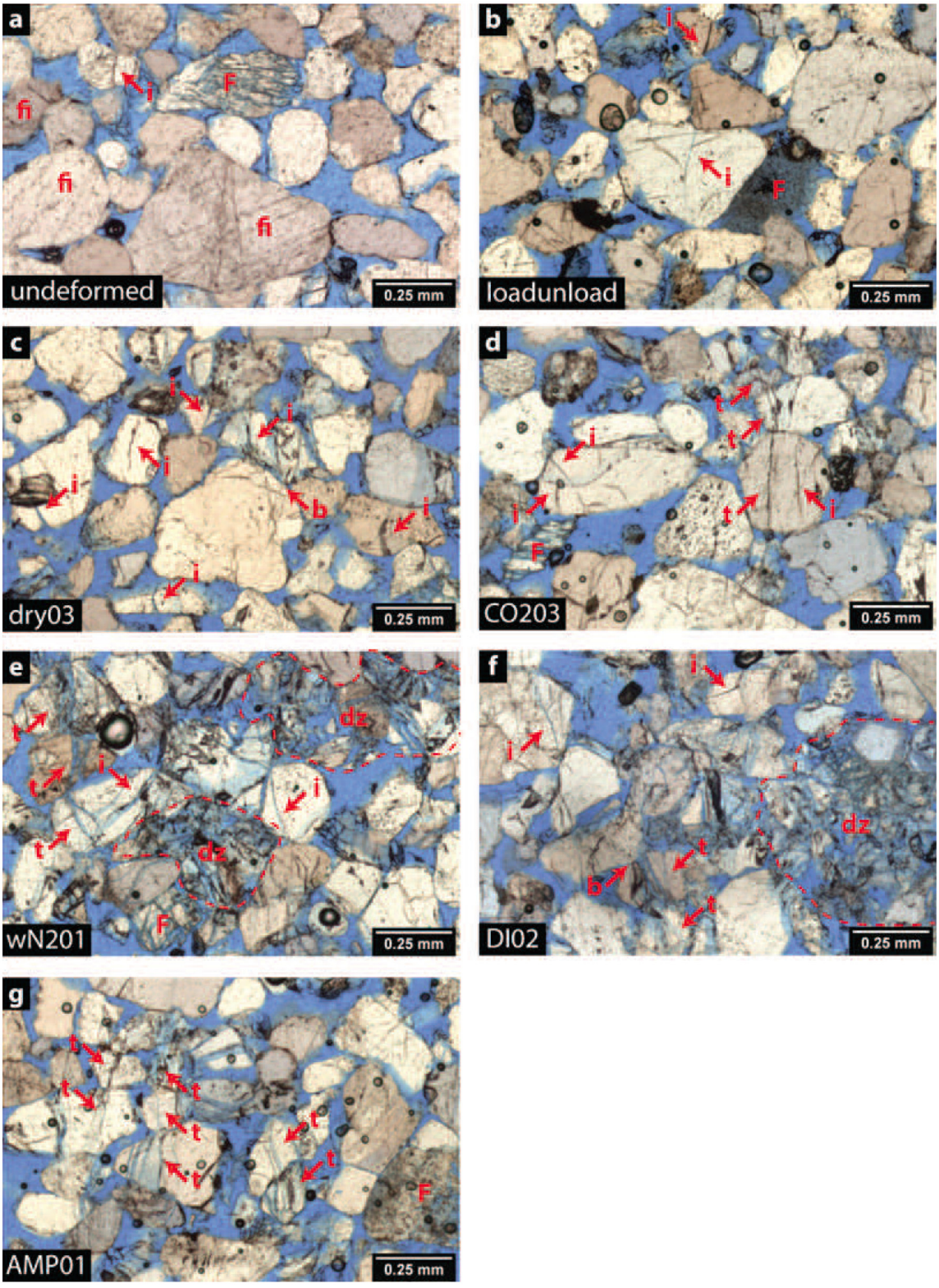

Fig. 8. Transmitted light micrographs showing the microstructure of Bentheim sandstone samples. (a) Undeformed state. (b) After loading to 100 MPa applied stress under low-vacuum (dry) conditions and directly unloading. (c) After compaction creep at 100 MPa applied effective stress under low-vacuum (dry) conditions. (d–g) Samples tested under same conditions (100 MPa effective stress), but saturated with (d) CO_2, (e) wet-N_2, (f) distilled water, and (g) AMP solution. The loading direction is vertical. Examples of key microstructural features are indicated by arrows, where the letters indicate the following, F: (corroded) feldspar grains, fi: grain with fluid inclusions, i: intergranular crack, b: grain boundary breakage, t: transgranular crack, dz: damage zone with intense grain fracturing.

(i.e. no drying agent is added) and any water remaining in the system, e.g. water adsorbed on clay mineral surfaces present in the sandstone or on the detrital grain surfaces, could provide water that adsorbs onto crack tips, facilitating subcritical crack growth. Upon the introduction of dry supercritical N_2 and CO_2, it is likely that crack tips are dried, as free and even adsorbed water

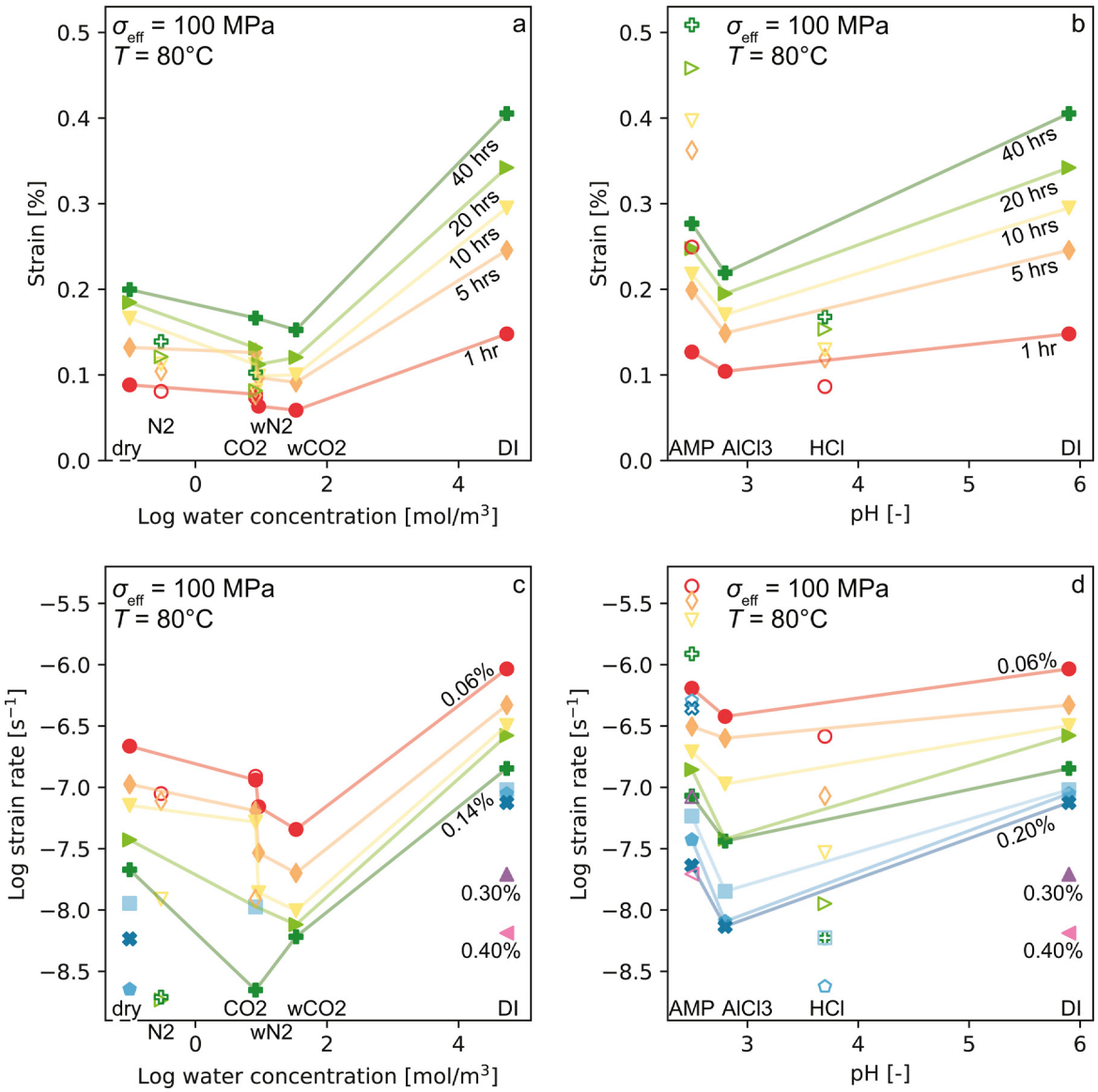

Fig. 9. (a and b) Strain at fixed moments in time, i.e. after 1, 5, 10, 20 and 40 h of compaction creep, as a function of log water concentration and pH. (c and d) Strain rate at fixed strains as a function of log water concentration and pH. Strain is shown for intervals of 0.02% between 0.06% and 0.20% strain, as well as 0.30 and 0.40% strain. Solid symbols represent samples within porosity range of 22.2–22.5% and are connected by tie lines, open symbols are samples falling outside this range. T denotes temperature and σ_{eff} effective stress. Letters indicate the following, dry: low-vacuum (dry) conditions, N2: saturated with N_2, CO2: saturated with CO_2, wN2: saturated with wet-N_2, wCO2: saturated with wet-CO_2, DI: saturated with distilled water, AMP: saturated with AMP solution, AlCl3: saturated with $AlCl_3$ solution, HCl: saturated with 3.7 HCl solution.

is being taken up by the supercritical phases.[79,80] Considering the purity of the dry N_2 and CO_2 (see Section 2.1), these phases would contain 0.3 and 8.2 mol water/m^3 and may potentially dissolve up to 19.4 and 66.7 mol water/m^3 at 80 °C and 10 MPa pore pressure, respectively. In turn, drying of the crack tips may prevent crack tip corrosion and inhibit compaction creep (see also Ref. 8 for creep experiments on pure quartz sand under the same conditions).

In the case of water-saturated supercritical phases, our experiments showed that these also inhibited compaction creep compared to low-vacuum (dry) conditions. This is contrary to the results reported by Ref. 8 who found that creep strain rates in quartz sand increased with increasing water content in the tested supercritical phases (N_2, CO_2 and wet-CO_2). In the current experiments, the supercritical phases were prepared at 60 °C to avoid water condensation upon introduction to the sample at 80 °C. This temperature difference leaves some room for water dissolution in the supercritical phase, i.e. 10.3 and 32.9 mol water/m^3 in case of the wet-N_2 and wet-CO_2, respectively (see Refs. 8, 78–80). Therefore, it is likely the water-saturated N_2 and CO_2 phases at 60 °C still had some drying potential at 80 °C and inhibited crack growth and sandstone compaction creep in the wet supercritical phases compared to low-vacuum (dry) conditions.

4.1.3. The influence of aqueous solutions on compaction creep

The influence of aqueous solutions on Bentheim sandstone compaction is illustrated in Fig. 9, where strain at fixed moments in time and strain rates at fixed strains is plotted as a function of solution pH. From these graphs, it is clear that for similar porosity samples, creep strain and strain rates tended to be lower for the acidic solutions than for distilled water. Enhanced compaction creep, AE count, creep strain rates and AE rates by the flooding with distilled water (Fig. 4) or aqueous solution, compared to dry conditions, is as expected if subcritical crack growth dominates deformation.[112–116] The strong water-weakening effect was also demonstrated by the zones of intense deformation (Fig. 8e and f)

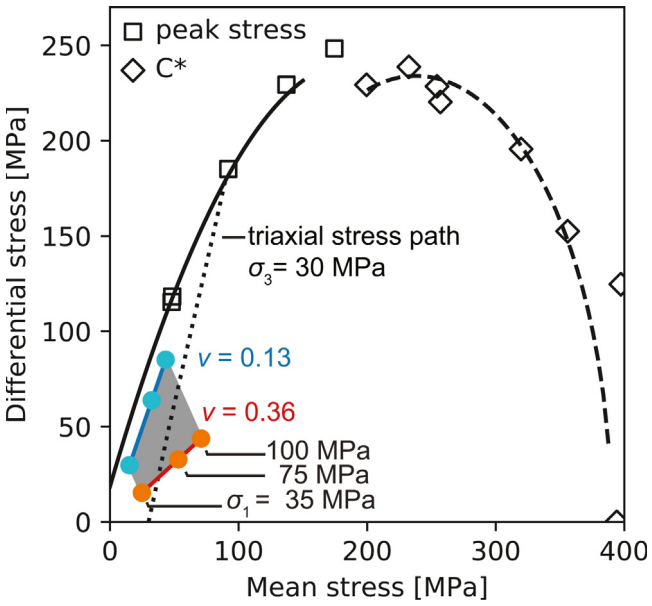

Fig. 10. Yield envelope of Bentheim sandstone with the solid line representing the shear failure envelope outlined by peak stress and the dashed line the shear-enhanced compaction endcap, as outlined by C* (plotted after Klein et al.[63]). Superimposed onto this yield envelope are the stress conditions relevant for our sandstone creep experiments, assuming laterally confined conditions with zero radial strain and zero initial radial stress and taking Poisson's ratio ν = 0.13–0.36. Solid markers indicate the effective stresses of 35, 75 and 100 MPa employed in the experiments. A typical stress path for a conventional triaxial experiment with a confining pressure (fixed radial stress) of 30 MPa is added for reference (dotted line).

that were observed in all samples saturated with distilled water or aqueous solution (except for sample HCl301). Interestingly, such a zone was also observed in the sample saturated with wet-N_2, which was eventually wetted with distilled water (Fig. 8e). We infer that the damage zone observed in sample wN201 was caused by the ingress of water, as none of the other supercritical phases displayed these microstructural features.

For glass and quartz, it is typically inferred that microcracking is inhibited in acidic solutions due to the (near) neutral surface charge at low pH.[99,106,117,118] In solution, adsorption causes the quartz surface to be covered by positively ($SiOH_2^+$) and negatively (SiO^-) charged surface complexes. Depending on solution pH, positive groups or negative groups dominate or they are balanced, resulting in a positively, negatively or neutrally charged surface, respectively.[105,124,125] For quartz, the pH of zero surface charge (pH_{PZC}) is approximately 2–3 at room temperature,[126,127] and is expected to be relatively temperature insensitive.[128] The neutrally charged quartz surface does not actively attract corrosive species and stress corrosion microcracking is, therefore, not promoted. At solution pH > pH_{PZC}, the quartz surface becomes increasingly more populated by negative surface complexes (SiO^-) and a negative surface charge develops, promoting the attraction of corrosive species such as water and hydroxyl molecules. Their interaction with crack tips (see Section 4.2) will weaken the Si-O bonds of the quartz and, hence, promote stress corrosion microcracking. This rate-controlling effect of pH on crack velocities is observed in glass and quartz[99,106,117,118] and in compaction creep tests on quartz sand aggregates.[8] However, for sandstone, a composite of quartz grains and other minerals, this influence of solution pH on crack propagation may be more complex, as each mineral has its own pH_{PZC}, i.e. for feldspar pH_{PZC} = 5-7,[129] and for clay minerals such as kaolinite pH_{PZC} = 5.6–6.6,[130] while for illite and montmorillonite pH_{PZC} = 9-10.[130]

Measurements of the average pH_{PZC} of Bentheim sandstone have suggested that the pH_{PZC} can range from 3[131] to 8.[65,66] For the lower value, it is suggested that the abundant presence of quartz controls the pH_{PZC} of the sandstone. For the high value, the measured pH_{PZC} is most likely dominated by the presence of thin iron oxide grain coatings,[66] which are typically characterised by higher a pH_{PZC} of 5–9.[126,127,132] Given the low amount and isolated occurrence of feldspar present in the sample material, it is unlikely that feldspar played a significant role in controlling the amount of deformation of our Bentheim samples, as also demonstrated by the widespread microcracking in quartz grains and across quartz grain contacts (Fig. 8). Therefore, we infer that it is the local pH_{PZC} of quartz that controls fluid-crack-tip-interactions rather than the macroscopic pH_{PZC} for Bentheim sandstone as a whole. The inhibiting effect of the acidic solutions on compaction creep may therefore reflect a reduced interaction between corrosive species and crack tips caused by near neutral surface charge.

Superimposed on the direct effect of solution pH, is the effect of the chemical species in solution. While it has been demonstrated that AMP and $AlCl_3$ solutions inhibited creep in quartz grains, they did not do so as effectively as a simple HCl solution of similar pH.[8] In case of the AMP solution, it has been inferred that due to incomplete dissociation of the AMP molecule (which consists of six hydroxyl groups[133]), some hydroxyl groups are left to attack the strained crack tips. By contrast, for quartz grains in contact with acidic $AlCl_3$ solution, Al^{3+} adsorption onto the quartz surface is believed to create a disordered surface-solvent structure, thereby allowing easier access of corrosive species to the crack tip.[124] Unfortunately we were not able to assess the effect on creep behaviour of HCl compared to AMP and $AlCl_3$ due to small porosity variations between the samples. However, it is not unlikely that the same trend observed for creep in sands[8] also apply to sandstone, as deformation of the former is also controlled by subcritical crack growth.

4.2. Sample boundary conditions and stress state evolution

Regarding the control experiments on aluminium samples, the measurement of the unconstrained stiffness (70 GPa) corresponds well with the expected value of E (69 ± 1 GPa – see Section 2.3.1), while the measurement of the constrained stiffness (144 GPa) overestimates the expected value of M (105 ± 4 GPa – see Section 2.3.1) by 37%. On this basis, we infer that the FEP-sleeve successfully constrained the tightly fitting aluminium sample to zero lateral strain at axial stresses above approximately 30 MPa.

In case of the Bentheim sandstone samples of similar porosity (22.3%) and loaded under low-vacuum (dry) conditions, the characteristic stiffness of the unconstrained sample was 7.0 ± 0.0 GPa, while the two constrained samples had higher stiffness values of 10.1 ± 0.0 GPa (loadunload) and 7.9 ± 0.1 GPa (dry02 – see Table 1). Various values for the unconstrained Young's modulus are described in the literature, ranging from 8.9 to 14.7 GPa.[65,67,75] Our measured value of the unconstrained sample stiffness is slightly below this range. The constrained modulus, calculated using Eq. (1) and assuming E is 8.9–14.7 GPa and υ is 0.13–0.36,[65,67,75] is expected to lie in the range 9.3–17.6 GPa. Our measured values of M fall below and within this range. Interestingly, the unconstrained sample failed around 62 MPa applied stress, while none of the constrained samples did. The unconfined compressive strength (UCS) of Bentheim sandstone reported in the literature is lower than our measured UCS and varies between 30 and 40 MPa.[65,67,75] The discrepancies between our measured data and the literature values could be caused by the aspect length:diameter ratio of our samples, which is 1:2, as opposed to the more conventional 2:1.[134] This could have led to stress

concentrations and clamping at the end of the sample, leading to higher failure stresses and lower sample stiffness. Considering both the difference in measured characteristic stiffness between unconstrained and constrained samples and the failure of the unconstrained sample, suggests that the FEP-sleeve approach effectively constrained the sandstone samples to zero lateral strain conditions at axial stresses above approximately 30 MPa.

Assuming our samples were laterally constrained, application of an axial stress (σ_1) to the sample led to the development of lateral or horizontal stresses ($\sigma_2 = \sigma_3$). Assuming pure poroelastic behaviour at constant pore fluid pressure, and assuming zero lateral strain conditions, the lateral stresses can be predicted according to[25]

$$\sigma_3 = \frac{\sigma_1}{\left(\frac{1}{\nu} - 1\right)} \tag{4}$$

With the Poisson's ratio of Bentheim sandstone ranging from 0.13 to 0.36,[65,67,75] σ_3 is predicted to be 12 $\pm$7, 27$\pm$ 15 and 36 $\pm$ 21 MPa for an applied effective stress of 35, 75 and 100 MPa, respectively. When plotted in conventional differential stress ($\sigma_1 - \sigma_3$) versus mean stress ($(\sigma_1 + 2\sigma_3)/3$) space, together with the failure envelope of Bentheim sandstone,[63] it can be seen that for all experiments the stress conditions were well below the failure condition (Fig. 10).

4.3. Implications

The results presented in this study may have several implications regarding fluid injection into porous subsurface reservoirs at 2–4 km depth, where microcracking is likely to contribute to reservoir deformation, specifically when stress conditions are perturbed to provide a drive for compaction creep. We envisage that the life-time of a grain is controlled by the rate at which cracks grow, so that injection of supercritical or acidic fluids increases the time-to-failure of the material and therefore slows creep.

Firstly, our results suggest that fluid injection into depleted, quartz-rich hydrocarbon reservoirs where the vertical effective stress has been increased by production, may be a suitable mitigation strategy for reducing long-term reservoir compaction. Injection of pressurised fluids will lower the effective stress acting on the reservoir rock, thereby reducing the driving force for reservoir compaction. In addition to this mechanical effect, a chemical effect is expected as well. For example, injection of supercritical phases that are devoid of water or contain trace water will tend to desiccate crack tips when the original water content is low, thereby reducing reservoir compaction creep rates by subcritical crack growth. In addition, injection of acidic fluids is likely to decelerate compaction creep rates, as the concomitant change in quartz surface energy will reduce subcritical crack growth rates. However, more research is needed to investigate the effect of (acidic) fluids on the compaction of impure sandstones having a larger feldspar, carbonate and clay content. Depending on the load-bearing framework, dissolution of carbonate cements on the short-term and feldspar grains on the long-term, by acidification of the pore fluid, may weaken the reservoir rock.[123,135,136]

Secondly, porous subsurface reservoirs, such as depleted hydrocarbon reservoirs, are envisioned as potential systems for permanently storing CO_2 and for temporary storage of renewably derived energy in the form of synthetic fuels, compressed air and hydrogen.[11] In the corresponding injection operations, it is important to avoid or minimise long-term reservoir compaction and creep effects, as these may cause induced seismicity and surface subsidence.[3,4,137] For efficiency reasons, most fuels injected will be devoid of water or contain trace amounts of water. Our experiments employing dry and wet supercritical phases may be regarded as representative of these injection scenarios and would suggest that, in case of injection into quartz-rich reservoirs, reservoir compaction would be not be enhanced, or perhaps even inhibited, by the injection of fluids and concomitant further (local) drying of the reservoir. Furthermore, the injection of CO_2 has the added advantage of contributing to reducing anthropogenic CO_2 emissions.[138]

Thirdly, geothermal energy production for renewable heat and electricity production also requires the injection of cold fluids that are in chemical disequilibrium with the receiving reservoir rock. These fluids would typically contain anti-scaling additives, such as AMP, or be acidic in nature,[139,140] enhancing any disequilibrium effects. During geothermal energy production, the injected and produced fluid volumes are balanced to maintain an approximately constant pore pressure in the reservoir. However, as the injected fluid will be relatively cold, the reservoir rock will be cooled, resulting in contraction of the reservoir rock and a decrease in the lateral stresses. Consequently, the differential stress acting on the reservoir rock will increase, which could provide a driving force for stress corrosion cracking. In addition, the tendency for stress corrosion cracking may be triggered by the change in chemical environment. Our experiments employing acidic solutions, including AMP, suggest that the rate of stress corrosion cracking would decrease, thereby inhibiting compaction creep, compared to injection with pure water. However, as described above, our research focused on the compaction behaviour of relatively clean sandstone, i.e. 95% quartz, and more research is needed to assess the effect of (acidic) fluids on sandstones with a higher feldspar, carbonate or clay content. Acidification of the pore fluid may lead to weakening in impure sandstones through reaction of feldspars and clays,[123,135,136] which could affect transport properties and, thereby, impact the performance of the geothermal reservoir.

Lastly, concerning the injection of fluids for energy storage, we only looked at the scenario of a fixed applied, or overburden stress. However, in an energy storage project, most likely pore pressure will fluctuate during production, decreasing when energy is produced and increasing when energy is stored. This would mean that such energy storage systems will go through many stress-cycles throughout their lifetime. In our current study, we did not investigate the effect of stress-cycling on creep or hysteresis. However, our stiffness data collected during active pre-creep loading may be representative of injection during the first stress-cycle. Sample stiffness displayed a small dependency on water concentration and no effect of fluid pH was observed, while sample porosity did influence sample stiffness. This implies that during the first phases of fluid injection and extraction, the porosity of the reservoir rock rather than pore fluid chemistry is likely to control reservoir compaction. After the first stress-cycle, additional permanent deformation is unlikely to develop, as, depending on the rate of the stress-cycle, only a small number of new cracks will form as long as the effective stress does not exceed the maximum previously achieved stress. With prolonged injection and extraction-cycling, time-dependent chemical processes such as dissolution and subcritical crack growth are likely to have a stronger contribution to reservoir compaction and pore fluid chemistry will have a more pronounced influence on compaction rates.

5. Conclusions

Uniaxial compaction experiments were performed using samples of Bentheim sandstone saturated with supercritical fluids and aqueous solutions of different pH and composition to investigate the effects of pore fluid chemistry on (near) 1-D compaction of reservoir sandstones, at realistic in situ reservoir conditions

(80 °C, effective axial stresses of 35, 75 and 100 MPa). The tested pore fluid environments included supercritical N_2, CO_2, wet-N_2 and wet-CO_2 at 10 MPa pore pressure, distilled water, pH 3.7 HCl solution, AMP-solution and $AlCl_3$-solution at atmospheric pressure, as well as, low-vacuum (dry) conditions. The following observations and inferences were made:

1. During loading, the stiffness of Bentheim sandstone samples was independent of water content in the pore fluid and solution pH. On the other hand, sample porosity appeared to exert an influence, as more porous samples were more compliant.
2. During the creep phase, compaction creep strain, AE count, creep strain rates and AE rates measured in low-vacuum (dry) and water-saturated (distilled water) samples increased with increasing applied stress. In addition, a clear effect of pore fluid chemistry was observed. Creep rate and AE rate increased moving from dry and wet supercritical N_2 and CO_2 phases, to low-vacuum (dry) conditions, to acidic aqueous solutions, to distilled water. Samples saturated with the same pore fluid but with different porosity had quantitatively different compaction behaviour. More porous samples produced more strain and AEs, which was accompanied by higher strain rates and AE rates.
3. It was inferred that compaction creep in Bentheim sandstone was controlled by subcritical crack growth by stress corrosion cracking, which is rate-dependent on the intergranular stresses and pore fluid chemistry. In turn, the rate of subcritical crack growth controls the rate of grain failure and, hence, compaction creep. Increasing the applied stress leads to larger stress concentrations at crack tips. In addition, in the more porous samples, grain-to-grain contacts were likely smaller or possessed a different structure or lower degree of cementation, such that the intergranular stresses were larger, promoting crack growth. Whereas saturation with the supercritical N_2 and CO_2 phases was inferred to actively dry crack tips and inhibit crack growth, saturation with distilled water fully wetted the crack tips, reducing the energy required for Si-O bond breakage and facilitating subcritical crack growth. In the case of saturation of acidic fluids, pH-dependent fluid–rock interactions were inferred to lower the rate of stress corrosion cracking.
4. Regarding fluid injection into quartz-rich, subsurface reservoirs characterised by ongoing reservoir compaction, the results imply that fluids devoid of water or with a minor amount of water, e.g. supercritical phases, may be injected to mitigate reservoir compaction. Injection of acidic fluids is also likely to inhibit reservoir compaction. However, this study focused on the compaction behaviour of relatively clean sandstone, i.e. 95% quartz, and more research is needed to assess the effect of fluids on sandstones with a higher feldspar, carbonate or clay content.

CRediT authorship contribution statement

M.T.W. Schimmel: Conceptualization, Methodology, Formal analysis, Investigation, Writing – original draft. **S.J.T. Hangx:** Conceptualization, Methodology, Writing – review & editing, Supervision. **C.J. Spiers:** Conceptualization, Methodology, Writing – review & editing, Supervision.

Declaration of competing interest

The authors declare that they have no known competing financial interests or personal relationships that could have appeared to influence the work reported in this paper.

Acknowledgements

This work is part of the research programme *Transitioning to a More Sustainable Energy System* with project number 022.004.023, which is financed by the Netherlands Organisation for Scientific Research (NWO).

We thank Dr. Natalie Farrell and an anonymous Reviewer for feedback on our manuscript. The technical staff of the HPT Laboratory is thanked for their assistance, especially Gerard Kuijpers, Thony van der Gon-Netscher and Floris van Oort. Leonard Bik is thanked for preparing the thin sections. We are thankful to Colin Peach and Tim Wolterbeek for assistance in the lab and constructive discussions.

References

1. Agency IE. *World Energy Outlook 2018*. OECD/IEA; 2018:661.
2. Suckale J. Moderate-to-large seismicity induced by hydrocarbon production. *The Leading Edge*. 2010;29(3):310–319. https://doi.org/10.1190/1.3353728.
3. Doornhof D, Kristiansen TG, Nagel NB, Patillo PD, Sayers C. Compaction and subsidence. *Oilfield Rev*. 2006; *Autumn*. 2006:50-68.
4. Nagel NB. Compaction and subsidence issues within the petroleum industry: From wilmington to ekofisk and beyond. *Phys Chem Earth A*. 2001;26(1):3–14. https://doi.org/10.1016/S1464-1895(01)00015-1.
5. Dahm T, Krüger F, Stammler K, et al. The 2004 mw 4.4 Rotenburg, Northern Germany, earthquake and its possible relationship with gas recovery. *Bull Seismol Soc Am*. 2007;97(3):691–704. https://doi.org/10.1785/0120050149.
6. Thienen-Visser Kvan, Breunese JN. Induced seismicity of the groningen gas field: History and recent developments. *The Leading Edge*. 2015;34(6):664–671. https://doi.org/10.1190/tle34060664.1.
7. Colazas XC, Strehle RW. Chapter 6 subsidence in the Wilmington oil field, long beach, California, USA. In: Chilingarian GV, Donaldson EC, Yen TF, eds. *Developments in Petroleum Science*. Elsevier; 1995:285–335.
8. Schimmel MTW, Hangx SJT, Spiers CJ. Impact of chemical environment on compaction creep of quartz sand and possible geomechanical applications. *J Geophys Res: Solid Earth*. 2019;124(6):5584–5606. https://doi.org/10.1029/2019JB017464.
9. Limberger J, Boxem T, Pluymaekers M, et al. Geothermal energy in deep aquifers: A global assessment of the resource base for direct heat utilization. *Renew Sustain Energy Rev*. 2018;82:961–975. https://doi.org/10.1016/j.rser.2017.09.084.
10. Ferguson G. Deep injection of waste water in the western Canada sedimentary basin. *Ground Water*. 2015;53(2):187–194. https://doi.org/10.1111/gwat.12198.
11. Mahlia TMI, Saktisahdan TJ, Jannifar A, Hasan MH, Matseelar HSC. A review of available methods and development on energy storage; technology update. *Renew Sustain Energy Rev*. 2014;33:532–545. https://doi.org/10.1016/j.rser.2014.01.068.
12. Graves C, Ebbesen SD, Mogensen M, Lackner KS. Sustainable hydrocarbon fuels by recycling CO_2 and H_2O with renewable or nuclear energy. *Renew Sustain Energy Rev*. 2011;15(1):1–23. https://doi.org/10.1016/j.rser.2010.07.014.
13. Budt M, Wolf D, Span R, Yan J. A review on compressed air energy storage: Basic principles, past milestones and recent developments. *Appl Energy*. 2016;170:250–268. https://doi.org/10.1016/j.apenergy.2016.02.108.
14. Tarkowski R. Underground hydrogen storage: Characteristics and prospects. *Renew Sustain Energy Rev*. 2019;105:86–94. https://doi.org/10.1016/j.rser.2019.01.051.
15. Liu W, Ramirez A. State of the art review of the environmental assessment and risks of underground geo-energy resources exploitation. *Renew Sustain Energy Rev*. 2017;76:628–644. https://doi.org/10.1016/j.rser.2017.03.087.
16. Schimmel M, Liu W, Worrell E. Facilitating sustainable geo-resources exploitation: A review of environmental and geological risks of fluid injection into hydrocarbon reservoirs. *Earth-Sci Rev*. 2019;194:455–471. https://doi.org/10.1016/j.earscirev.2019.03.006.
17. Ellsworth WL. Injection-induced earthquakes. *Science*. 2013;341(6142):1225942. https://doi.org/10.1126/science.1225942.
18. Weingarten M, Ge S, Godt JW, Bekins BA, Rubinstein JL. High-rate injection is associated with the increase in U.S. mid-continent seismicity. *Science*. 2015;348(6241):1336. https://doi.org/10.1126/science.aab1345.
19. Gaucher E, Schoenball M, Heidbach O, et al. Induced seismicity in geothermal reservoirs: A review of forecasting approaches. *Renew Sustain Energy Rev*. 2015;52:1473–1490. https://doi.org/10.1016/j.rser.2015.08.026.
20. Zang A, Oye V, Jousset P, et al. Analysis of induced seismicity in geothermal reservoirs – An overview. *Geothermics*. 2014;52:6–21. https://doi.org/10.1016/j.geothermics.2014.06.005.

21. S.T. Anderson. Risk, liability, and economic issues with long-term CO_2 storage—A review. *Nat Resour Res*. 2017;26(1):89–112. https://doi.org/10.1007/s11053-016-9303-6.
22. Deng H, Bielicki JM, Oppenheimer M, Fitts JP, Peters CA. Leakage risks of geologic CO_2 storage and the impacts on the global energy system and climate change mitigation. *Clim Change*. 2017;144(2):151–163. https://doi.org/10.1007/s10584-017-2035-8.
23. Ko D, Yoo G, Yun S-T, Chung H. Impacts of CO_2 leakage on plants and microorganisms: A review of results from CO_2 release experiments and storage sites. *Greenh Gases: Sci Tech*. 2016;6(3):319–338. https://doi.org/10.1002/ghg.1593.
24. Qafoku NP, Lawter AR, Bacon DH, Zheng L, Kyle J, Brown CF. Review of the impacts of leaking CO_2 gas and brine on groundwater quality. *Earth-Sci Rev*. 2017;169:69–84. https://doi.org/10.1016/j.earscirev.2017.04.010.
25. H.F. Wang. *Theory of Linear Poroelasticity with Applications To Geomechanics and Hydrogeology*. Princeton University Press; 2000:287.
26. Santarelli FJ, Tronvoll JT, Svennekjaier M, Skeie H, Henriksen R, Bratli RK. *Reservoir Stress Path: The Depletion and the Rebound*. 1998.
27. Pijnenburg RPJ, Verberne BA, Hangx SJT, Spiers CJ. Inelastic deformation of the slochteren sandstone: Stress-strain relations and implications for induced seismicity in the groningen gas field. *J Geophys Res: Solid Earth*. 2019;124(5):5254–5282. https://doi.org/10.1029/2019jb017366.
28. Pijnenburg RPJ, Verberne BA, Hangx SJT, Spiers CJ. Deformation behavior of sandstones from the seismogenic groningen gas field: Role of inelastic versus elastic mechanisms. *J Geophys Res: Solid Earth*. 2018;123(7):5532–5558. https://doi.org/10.1029/2018jb015673.
29. Hol S, Mossop AP, Linden AJvander, Zuiderwijk PMM, Makurat AH. *Long-Term Compaction Behavior of Permian Sandstones - An Investigation Into the Mechanisms of Subsidence in the Dutch Wadden Sea*. 2015.
30. Hettema M, Papamichos E, Schutjens P. Subsidence delay: Field observations and analysis. *Oil & Gas Sci Technol - Rev IFP*. 2002;57(5):443–458.
31. Chuhan FA, Kjeldstad A, Bjørlykke K, Høeg K. Experimental compression of loose sands: relevance to porosity reduction during burial in sedimentary basins. *Can Geotech J*. 2003;40(5):995–1011. https://doi.org/10.1139/t03-050.
32. Mesri G, Vardhanabhuti B. Compression of granular materials. *Can Geotech J*. 2009;46(4):369–392. https://doi.org/10.1139/t08-123.
33. Takei M, Kusakabe O, Hayashi T. Time-dependent behavior of crushable materials in one-dimensional compression tests. *Soil Found*. 2001;41(1):97–121. https://doi.org/10.3208/sandf.41.97.
34. Omidvar M, Iskander M, Bless S. Stress–strain behavior of sand at high strain rates. *Int J Impact Eng*. 2012;49:192–213. https://doi.org/10.1016/j.ijimpeng.2012.03.004.
35. Brantut N, Baud P, Heap MJ, Meredith PG. Micromechanics of brittle creep in rocks. *J Geophys Res: Solid Earth*. 2012;117(B8). https://doi.org/10.1029/2012JB009299.
36. Brzesowsky RH, Spiers CJ, Peach CJ, Hangx SJT. Time-independent compaction behavior of quartz sands. *J Geophys Res: Solid Earth*. 2014;119(2):936–956. https://doi.org/10.1002/2013JB010444.
37. Brzesowsky RH, Hangx SJT, Brantut N, Spiers CJ. Compaction creep of sands due to time-dependent grain failure: Effects of chemical environment, applied stress, and grain size. *J Geophys Res: Solid Earth*. 2014;119(10):7521–7541. https://doi.org/10.1002/2014JB011277.
38. Spiers CJ, Hangx SJT, Niemeijer AR. New approaches in experimental research on rock and fault behaviour in the Groningen gas field. *Neth J Geosci*. 2017;96(5):s55–s69. https://doi.org/10.1017/njg.2017.32.
39. Schutjens PMTM. Experimental compaction of quartz sand at low effective stress and temperature conditions. *J Geol Soc*. 1991;148(3):527. https://doi.org/10.1144/gsjgs.148.3.0527.
40. Rate laws for water-assisted compaction and stress-induced water-rock interaction in sandstones. *J Geophys Res: Solid Earth*. 1995;100(7):13093–13112. https://doi.org/10.1029/95JB00912.
41. Spiers CJ, Meer SDe, Niemeijer AR, Zhang X. Kinetics of rock deformation by pressure solution and the role of thin aqueous films. In: Nakashima S, Spiers CJ, Mercury L, Fenter PA, Hochella JMF, eds. *Physicochemistry of Water in Geological and Biological Systems*. 44th ed. Universal Academy Press, Inc.; 2004:129–158. In: Frontiers Science Series.
42. Gratier J-P, Guiguet R, Renard F, Jenatton L, Bernard D. A pressure solution creep law for quartz from indentation experiments. *J Geophys Res: Solid Earth*. 2009;114(B3). https://doi.org/10.1029/2008JB005652.
43. Dove PM. The dissolution kinetics of quartz in aqueous mixed cation solutions. *Geochim Cosmochim Acta*. 1999;63(22):3715–3727. https://doi.org/10.1016/S0016-7037(99)00218-5.
44. Hajash A, Carpenter TD, Dewers TA. Dissolution and time-dependent compaction of albite sand: experiments at 100 °C and 160 °C in pH-buffered organic acids and distilled water. *Tectonophysics*. 1998;295(1):93–115. https://doi.org/10.1016/S0040-1951(98)00117-6.
45. Hangx SJT, Spiers CJ, Peach CJ. Creep of simulated reservoir sands and coupled chemical–mechanical effects of CO_2 injection. *J Geophys Res: Solid Earth*. 2010;115(B9). https://doi.org/10.1029/2009JB006939.
46. Chester JS, Lenz SC, Chester FM, Lang RA. Mechanisms of compaction of quartz sand at diagenetic conditions. *Earth Planet Sci Lett*. 2004;220(3):435–451. https://doi.org/10.1016/S0012-821X(04)00054-8.
47. Chester FM, Chester JS, Kronenberg AK, Hajash A. Subcritical creep compaction of quartz sand at diagenetic conditions: Effects of water and grain size. *J Geophys Res: Solid Earth*. 2007;112(B6). https://doi.org/10.1029/2006JB004317.
48. Schimmel MTW, Hangx SJT, Spiers CJ. Impact of chemical environment on compaction behaviour of quartz sands during stress-cycling. *Rock Mech Rock Eng*. 2021;54(3):981–1003. https://doi.org/10.1007/s00603-020-02267-0.
49. Zhang Y, Xu W-y, Gu J-j, Wang W. Triaxial creep tests of weak sandstone from fracture zone of high dam foundation. *J Cent South Univ*. 2013;20(9):2528–2536. https://doi.org/10.1007/s11771-013-1765-7.
50. Rutter EH, Mainprice DH. The effect of water on stress relaxation of faulted and unfaulted sandstone. *Pure Appl Geophys*. 1978;116(4):634–654. https://doi.org/10.1007/BF00876530.
51. Ojala IO, Ngwenya BT, Main IG, Elphick SC. Correlation of microseismic and chemical properties of brittle deformation in Locharbriggs sandstone. *J Geophys Res: Solid Earth*. 2003;108(5). https://doi.org/10.1029/2002JB002277.
52. Yang S-Q, Jing H-W, Cheng L. Influences of pore pressure on short-term and creep mechanical behavior of red sandstone. *Eng Geol*. 2014;179:10–23. https://doi.org/10.1016/j.enggeo.2014.06.016.
53. Heap MJ, Reuschlé T, Kushnir ARL, Baud P. The influence of hydrothermal brine on the short-term strength and elastic modulus of sandstones from exploration well EPS-1 at Soultz-sous-Forêts (France). *Geotherm Energy*. 2018;6(1):29. https://doi.org/10.1186/s40517-018-0116-1.
54. Hol S, van der Linden A, Bierman S, Marcelis F, Makurat A. Rock physical controls on production-induced compaction in the groningen field. *Sci Rep*. 2018;8(1):7156. https://doi.org/10.1038/s41598-018-25455-z.
55. Heap MJ, Baud P, Meredith PG. Influence of temperature on brittle creep in sandstones. *Geophys Res Lett*. 2009;36(19). https://doi.org/10.1029/2009GL039373.
56. Heap MJ, Baud P, Meredith PG, Bell AF, Main IG. Time-dependent brittle creep in darley dale sandstone. *J Geophys Res: Solid Earth*. 2009;114(B7). https://doi.org/10.1029/2008JB006212.
57. Ngwenya BT, Main IG, Elphick SC, Crawford BR, Smart BGD. A constitutive law for low-temperature creep of water-saturated sandstones. *J Geophys Res: Solid Earth*. 2001;106(10):21811–21826. https://doi.org/10.1029/2001JB000403.
58. Baud P, Meredith PG. Damage accumulation during triaxial creep of darley dale sandstone from pore volumometry and acoustic emission. *Int J Rock Mech Min Sci*. 1997;34(3):24.e1–24.e10. https://doi.org/10.1016/S1365-1609(97)00060-9.
59. Tsai LS, Hsieh YM, Weng MC, Huang TH, Jeng FS. Time-dependent deformation behaviors of weak sandstones. *Int J Rock Mech Min Sci*. 2008;45(2):144–154. https://doi.org/10.1016/j.ijrmms.2007.04.008.
60. Yang S, Jiang Y. Triaxial mechanical creep behavior of sandstone. *Min Sci Technol (China)*. 2010;20(3):339–349. https://doi.org/10.1016/S1674-5264(09)60206-4.
61. Brantut N, Heap MJ, Meredith PG, Baud P. Time-dependent cracking and brittle creep in crustal rocks: A review. *J Struct Geol*. 2013;52:17–43. https://doi.org/10.1016/j.jsg.2013.03.007.
62. Segall P, Fitzgerald SD. A note on induced stress changes in hydrocarbon and geothermal reservoirs. *Tectonophysics*. 1998;289(1):117–128. https://doi.org/10.1016/S0040-1951(97)00311-9.
63. Klein E, Baud P, Reuschlé T, Tf Wong. Mechanical behaviour and failure mode of bentheim sandstone under triaxial compression. *Phys Chem Earth A*. 2001;26(1):21–25. https://doi.org/10.1016/S1464-1895(01)00017-5.
64. Klein E, Reuschlé T. A model for the mechanical behaviour of bentheim sandstone in the brittle regime. *Pure Appl Geophys*. 2003;160(5):833–849. https://doi.org/10.1007/PL00012568.
65. Peksa AE, Wolf K-HAA, Zitha PLJ. Bentheimer sandstone revisited for experimental purposes. *Mar Pet Geol*. 2015;67:701–719. https://doi.org/10.1016/j.marpetgeo.2015.06.001.
66. Peksa AE, Wolf K-HAA, Slob EC, Chmura Ł, Zitha PLJ. Original and pyrometamorphical altered bentheimer sandstone; petrophysical properties, surface and dielectric behavior. *J Pet Sci Eng*. 2017;149:270–280. https://doi.org/10.1016/j.petrol.2016.10.024.
67. Heap MJ, Faulkner DR, Meredith PG, Vinciguerra S. Elastic moduli evolution and accompanying stress changes with increasing crack damage: implications for stress changes around fault zones and volcanoes during deformation. *Geophys J Int*. 2010;183(1):225–236. https://doi.org/10.1111/j.1365-246X.2010.04726.x.
68. Stanchits S, Fortin J, Gueguen Y, Dresen G. Initiation and propagation of compaction bands in dry and wet bentheim sandstone. *Pure Appl Geophys*. 2009;166(5):843–868. https://doi.org/10.1007/s00024-009-0478-1.

69. Louis L, David C, Metz V, Robion P, Menéndez B, Kissel C. Microstructural control on the anisotropy of elastic and transport properties in undeformed sandstones. *Int J Rock Mech Min Sci*. 2005;42(7):911–923. https://doi.org/10.1016/j.ijrmms.2005.05.004.
70. Wong T-f, Baud P, Klein E. Localized failure modes in a compactant porous rock. *Geophys Res Lett*. 2001;28(13):2521–2524. https://doi.org/10.1029/2001GL012960.
71. Baud P, Klein E, Wong T-f. Compaction localization in porous sandstones: spatial evolution of damage and acoustic emission activity. *J Struct Geol*. 2004;26(4):603–624. https://doi.org/10.1016/j.jsg.2003.09.002.
72. Tembe S, Baud P, Wong T-f. Stress conditions for the propagation of discrete compaction bands in porous sandstone. *J Geophys Res: Solid Earth*. 2008;113(B9). https://doi.org/10.1029/2007JB005439.
73. Baud P, Vajdova V, Wong T-f. Shear-enhanced compaction and strain localization: Inelastic deformation and constitutive modeling of four porous sandstones. *J Geophys Res: Solid Earth*. 2006;111(12). https://doi.org/10.1029/2005JB004101.
74. Vajdova V, Wong T-F. Incremental propagation of discrete compaction bands: Acoustic emission and microstructural observations on circumferentially notched samples of bentheim. *Geophys Res Lett*. 2003;30(14). https://doi.org/10.1029/2003GL017750.
75. Ma X, Haimson BC. Failure characteristics of two porous sandstones subjected to true triaxial stresses. *J Geophys Res: Solid Earth*. 2016;121(9):6477–6498. https://doi.org/10.1002/2016JB012979.
76. Ma X, Rudnicki JW, Haimson BC. Failure characteristics of two porous sandstones subjected to true triaxial stresses: Applied through a novel loading path. *J Geophys Res: Solid Earth*. 2017;122(4):2525–2540. https://doi.org/10.1002/2016JB013637.
77. Brantut N, Heap MJ, Baud P, Meredith PG. Rate- and strain-dependent brittle deformation of rocks. *J Geophys Res: Solid Earth*. 2014;119(3):1818–1836. https://doi.org/10.1002/2013JB010448.
78. Lemmon EW, McLinden MO, Friend DG. Thermophysical properties of fluid systems. In: NIST Chemistry WebBook, NIST standard reference database number 69.
79. Sun R, Lai S, Dubessy J. Calculations of vapor–liquid equilibria of the H_2O-N_2 and H_2O-H_2 systems with improved SAFT-LJ EOS. *Fluid Phase Equilib*. 2015;390:23–33. https://doi.org/10.1016/j.fluid.2015.01.018.
80. Sun R, Dubessy J. Prediction of vapor–liquid equilibrium and PVTx properties of geological fluid system with SAFT-LJ EOS including multi-polar contribution. Part II: Application to H_2O–NaCl and CO_2–H_2O–NaCl system. *Geochim Cosmochim Acta*. 2012;88:130–145. https://doi.org/10.1016/j.gca.2012.04.025.
81. Vilamosa V, Clausen AH, Børvik T, Holmedal B, Hopperstad OS. A physically-based constitutive model applied to AA6082 aluminium alloy at large strains, high strain rates and elevated temperatures. *Mater Des*. 2016;03:391–405. https://doi.org/10.1016/j.matdes.2016.04.047.
82. Pereira AM, Ferreira JM, Antunes FV, Bártolo PJ. Study on the fatigue strength of AA 6082-T6 adhesive lap joints. *Int J Adhes Adhes*. 2009;29(6):633–638. https://doi.org/10.1016/j.ijadhadh.2009.02.009.
83. Semari Z, Aid A, Benhamena A, et al. Effect of residual stresses induced by cold expansion on the crack growth in 6082 aluminum alloy. *Eng Fract Mech*. 2013;99:159–168. https://doi.org/10.1016/j.engfracmech.2012.12.003.
84. Niemeijer AR, Spiers CJ, Bos B. Compaction creep of quartz sand at 400–600 °C: experimental evidence for dissolution-controlled pressure solution. *Earth Planet Sci Lett*. 2002;195(3):261–275. https://doi.org/10.1016/S0012-821X(01)00593-3.
85. Zhang J, Wong T-F, Davis DM. Micromechanics of pressure-induced grain crushing in porous rocks. *J Geophys Res: Solid Earth*. 1990;95(1). https://doi.org/10.1029/JB095iB01p00341.
86. Menéndez B, Zhu W, Wong T-F. Micromechanics of brittle faulting and cataclastic flow in Berea sandstone. *J Struct Geol*. 1996;18(1):1–16. https://doi.org/10.1016/0191-8141(95)00076-P.
87. Hertz H. *Ueber die Berührung fester elastischer Körper*. 1882;92:156–171. https://doi.org/10.1515/crll.1882.92.156.
88. Wong T-F, Wu L-C. Tensile stress concentration and compressive failure in cemented granular material. *Geophys Res Lett*. 1995;22(13):1649–1652. https://doi.org/10.1029/95GL01596.
89. Rice JR. Thermodynamics of the quasi-static growth of Griffith cracks. *J Mech Phys Solids*. 1978;26(2):61–78. https://doi.org/10.1016/0022-5096(78)90014-5.
90. Lawn BR. An atomistic model of kinetic crack growth in brittle solids. *J Mater Sci*. 1975;10(3):469–480. https://doi.org/10.1007/BF00543692.
91. Irwin GR. *Elasticity and Plasticity/Elastizität und Plastizität Handbuch der Physik/Encyclopedia of Physics*. Springer; 1958:642. chap 5,
92. Lawn B. *Fracture of Brittle Solids*. 2nd ed. Cambridge University Press; 1993. In: Cambridge Solid State Science Series.
93. Atkinson BK. Subcritical crack growth in geological materials. *J Geophys Res: Solid Earth*. 1984;89(6):4077–4114. https://doi.org/10.1029/JB089iB06p04077.
94. Griffith AA, Taylor GIVI. The phenomena of rupture and flow in solids. *Philos Trans R Soc Lond Ser A Math Phys Eng Sci*. 1921;221(582–593):163–198. https://doi.org/10.1098/rsta.1921.0006.
95. Orowan E. The fatigue of glass under stress. *Nature*. 1944;154(3906):341–343. https://doi.org/10.1038/154341a0.
96. Dunning J, Douglas B, Miller M, McDonald S. The role of the chemical environment in frictional deformation: Stress corrosion cracking and comminution. *Pure Appl Geophys*. 1994;143(1):151–178. https://doi.org/10.1007/BF00874327.
97. Fisk GA, Michalske TA. Laser-based and thermal studies of stress corrosion in vitreous silica. *J Appl Phys*. 1985;58(7):2736–2741. https://doi.org/10.1063/1.335860.
98. Michalske TA, Bunker BC. Slow fracture model based on strained silicate structures. *J Appl Phys*. 1984;56(10):2686–2693. https://doi.org/10.1063/1.333789.
99. Atkinson BK, Meredith PG. Stress corrosion cracking of quartz: A note on the influence of chemical environment. *Tectonophysics*. 1981;77(1):T1–T11. https://doi.org/10.1016/0040-1951(81)90157-8.
100. Lindsay CG, White GS, Freiman SW, Wong-Ng W. Molecular orbital study of an environmentally enhanced crack growth process in silica. *J Am Ceram Soc*. 1994;77(8):2179–2187. https://doi.org/10.1111/j.1151-2916.1994.tb07115.x.
101. Michalske TA, Freiman SW. A molecular interpretation of stress corrosion in silica. *Nature*. 1982;295(5849):511–512. https://doi.org/10.1038/295511a0.
102. Ciacchi LColombi, Cole DJ, Payne MC, Gumbsch P. Stress-driven oxidation chemistry of wet silicon surfaces. *J Phys Chem C*. 2008;112(32):12077–12080. https://doi.org/10.1021/jp804078n.
103. Silva ECCM, Li J, Liao D, Subramanian S, Zhu T, Yip S. Atomic scale chemo-mechanics of silica: Nano-rod deformation and water reaction. *J Comput Aided Mater Des*. 2006;13(1):135–159. https://doi.org/10.1007/s10820-006-9008-y.
104. Zhang Y-A, Tao J, Chen X, Liu B. Mixed-pattern cracking in silica during stress corrosion: A reactive molecular dynamics simulation. *Comput Mater Sci*. 2014;82:237–243. https://doi.org/10.1016/j.commatsci.2013.09.045.
105. Parks GA. Surface and interfacial free energies of quartz. *J Geophys Res: Solid Earth*. 1984;89(B6):3997–4008. https://doi.org/10.1029/JB089iB06p03997.
106. P.M. Dove. Geochemical controls on the kinetics of quartz fracture at subcritical tensile stresses. *J Geophys Res: Solid Earth*. 1995;100(B11):22349–22359. https://doi.org/10.1029/95JB02155.
107. Charles RJ. Static fatigue of glass. I. *J Appl Phys*. 1958;29(11):1549–1553. https://doi.org/10.1063/1.1722991.
108. Xiao Y, Lasaga A. Ab initio quantum mechanical studies of the kinetics and mechanisms of silicate dissolution: H+(H_3O+) catalysis. *Geochim Cosmochim Acta*. 1994;58:5379–5400.
109. Xiao Y, Lasaga AC. Ab initio quantum mechanical studies of the kinetics and mechanisms of quartz dissolution: OH- catalysis. *Geochim Cosmochim Acta*. 1996;60(13):2283–2295. https://doi.org/10.1016/0016-7037(96)00101-9.
110. Wiederhorn SM, Bolz LH. Stress corrosion and static fatigue of glass. *J Am Ceram Soc*. 1970;53(10):543–548. https://doi.org/10.1111/j.1151-2916.1970.tb15962.x.
111. Wiederhorn SM, Fuller ER, Thomson R. Micromechanisms of crack growth in ceramics and glasses in corrosive environments. *Met Sci*. 1980;14(8–9):450–458. https://doi.org/10.1179/msc.1980.14.8-9.450.
112. Wiederhorn SM, Freiman SW, Fuller ER, Simmons CJ. Effects of water and other dielectrics on crack growth. *J Mater Sci*. 1982;17(12):3460–3478. https://doi.org/10.1007/BF00752191.
113. Michalske TA, Freiman SW. A molecular mechanism for stress corrosion in vitreous silica. *J Am Ceram Soc*. 1983;66(4):284–288. https://doi.org/10.1111/j.1151-2916.1983.tb15715.x.
114. Atkinson BK. A fracture mechanics study of subcritical tensile cracking of quartz in wet environments. *Pure Appl Geophys*. 1979;117(5):1011–1024. https://doi.org/10.1007/BF00876082.
115. Scholz CH. Static fatigue of quartz. *J Geophys Res: Solid Earth (1896–1977)*. 1972;77(11):2104–2114. https://doi.org/10.1029/JB077i011p02104.
116. Wiederhorn SM. Influence of water vapor on crack propagation in soda-lime glass. *J Am Ceram Soc*. 1967;50(8):407–414. https://doi.org/10.1111/j.1151-2916.1967.tb15145.x.
117. Wiederhorn SM, Johnson H. Effect of electrolyte pH on crack propagation in glass. *J Am Ceram Soc*. 1973;56(4):192–197. https://doi.org/10.1111/j.1151-2916.1973.tb12454.
118. Dunning JD, Petrovski D, Schuyler J, Owens A. The effects of aqueous chemical environments on crack propagation in quartz. *J Geophys Res: Solid Earth*. 1984;89(6):4115–4123. https://doi.org/10.1029/JB089iB06p04115.
119. Swanson PL. Subcritical crack growth and other time- and environment-dependent behavior in crustal rocks. *J Geophys Res: Solid Earth*. 1984;89(B6):4137–4152. https://doi.org/10.1029/JB089iB06p04137.

120. Nara Y, Morimoto K, Yoneda T, Hiroyoshi N, Kaneko K. Effects of humidity and temperature on subcritical crack growth in sandstone. *Int J Solids Struct*. 2011;48(7):1130–1140. https://doi.org/10.1016/j.ijsolstr.2010.12.019.
121. Holder J, Olson JE, Philip Z. Experimental determination of subcritical crack growth parameters in sedimentary rock. *Geophys Res Lett*. 2001;28(4):599–602. https://doi.org/10.1029/2000GL011918.
122. Rijken M. *Modeling Naturally Fractured Reservoirs: From Experimental Rock Mechanics to Flow Simulation*. 2005.
123. Guen YL, Renard F, Hellmann R, et al. Enhanced deformation of limestone and sandstone in the presence of high pCO_2 fluids. *J Geophys Res*. 2007;112.
124. Du Q, Freysz E, Shen YR. Vibrational spectra of water molecules at quartz/water interfaces. *Phys Rev Lett*. 1994;72(2):238–241. https://doi.org/10.1103/PhysRevLett.72.238.
125. Dove PM, Elston SF. Dissolution kinetics of quartz in sodium chloride solutions: Analysis of existing data and a rate model for 25 °C. *Geochim Cosmochim Acta*. 1992;56(12):4147–4156. https://doi.org/10.1016/0016-7037(92)90257-J.
126. Parks GA. The isoelectric points of solid oxides, solid hydroxides, and aqueous hydroxo complex systems. *Chem Rev*. 1965;65(2):177–198. https://doi.org/10.1021/cr60234a002.
127. Kosmulski M. The pH dependent surface charging and points of zero charge. VII. Update. *Adv Colloid Interface Sci*. 2018;251:115–138. https://doi.org/10.1016/j.cis.2017.10.005.
128. Sverjensky DA, Sahai N. Theoretical prediction of single-site enthalpies of surface protonation for oxides and silicates in water. *Geochim Cosmochim Acta*. 1998;62(23):3703–3716. https://doi.org/10.1016/S0016-7037(98)00262-2.
129. Sverjensky DA. Zero-point-of-charge prediction from crystal chemistry and solvation theory. *Geochim Cosmochim Acta*. 1994;58(14):3123–3129. https://doi.org/10.1016/0016-7037(94)90184-8.
130. Hao W, Flynn SL, Alessi DS, Konhauser KO. Change of the point of zero net proton charge (pHPZNPC) of clay minerals with ionic strength. *Chem Geol*. 2018;493:458–467. https://doi.org/10.1016/j.chemgeo.2018.06.023.
131. Farooq U, Tweheyo MT, Sjöblom J, Øye G. Surface characterization of model, outcrop, and reservoir samples in low salinity aqueous solutions. *J Dispers Sci Technol*. 2011;32(4):519–531. https://doi.org/10.1080/01932691003756936.
132. Schwertmann U, Fechter H. The point of zero charge of natural and synthetic ferrihydrites and its relation to adsorbed silicate. *Clay Miner*. 1982;17(4):471–476. https://doi.org/10.1180/claymin.1982.017.4.10.
133. Tantayakom V, Fogler HS, Charoensirithavorn P, Chavadej S. Kinetic study of scale inhibitor precipitation in squeeze treatment. *Cryst Growth Des*. 2005;5(1):329–335. https://doi.org/10.1021/cg049874d.
134. Mogi K. *Experimental Rock Mechanics*. Taylor & Francis/Balkema; 2007.
135. Hangx S, Linden Avander, Marcelis F, Bauer A. The effect of CO_2 on the mechanical properties of the captain sandstone: Geological storage of CO_2 at the goldeneye field (UK). *Int J Greenh Gas Control*. 2013;19:609–619. https://doi.org/10.1016/j.ijggc.2012.12.016.
136. Rohmer J, Pluymakers A, Renard F. Mechano-chemical interactions in sedimentary rocks in the context of CO_2 storage: Weak acid, weak effects? *Earth-Sci Rev*. 2016;157:86–110. https://doi.org/10.1016/j.earscirev.2016.03.009.
137. Suckale J. Induced seismicity in hydrocarbon fields. *Adv Geophys*. 2009;51:55–106.
138. IPCC. *IPCC Special Report on Carbon Dioxide Capture and Storage. Prepared By Working Group III of the Intergovernmental Panel on Climate Change*. IPCC; 2005:442.
139. Finster M, Clark C, Schroeder J, Martino L. Geothermal produced fluids: Characteristics, treatment technologies, and management options. *Renew Sustain Energy Rev*. 2015;50:952–966. https://doi.org/10.1016/j.rser.2015.05.059.
140. Knepper TP. Synthetic chelating agents and compounds exhibiting complexing properties in the aquatic environment. *TRAC Trends Anal Chem*. 2003;22(10):708–724. https://doi.org/10.1016/S0165-9936(03)01008-2.